CHAPTER 4

THE ATOMISTIC GREEN'S FUNCTION METHOD FOR INTERFACIAL PHONON TRANSPORT

Sridhar Sadasivam,[1] Yuhang Che,[1] Zhen Huang,[2] Liang Chen,[3] Satish Kumar,[3] &
Timothy S. Fisher[1,] *

[1] Department of Mechanical Engineering and Birck Nanotechnology Center, Purdue University, West Lafayette, IN 47906

[2] IBM Corporation, Austin, TX 78758

[3] G.W. Woodruff School of Mechanical Engineering, Georgia Institute of Technology, Atlanta, GA 30318

*Address all correspondence to Timothy S. Fisher E-mail: tsfisher@purdue.edu

The atomistic Green's function method (AGF) has emerged as a useful tool to study phonon transport across interfaces. A comprehensive review of developments in the AGF method over the last decade is provided in this chapter. The content includes a discussion of the fundamentals of a Green's function starting from a continuum viewpoint and extending it to the atomistic regime. Comprehensive derivations of the AGF equations (within the harmonic framework) are presented along with intuitive physical explanations for the various matrices involved. The numerical issues in computational implementation of the various mathematical equations are illustrated with a one-dimensional atom chain example. The application of the AGF method to dimensionally mismatched and bulk interfaces and the process of obtaining polarization-specific transmission functions are illustrated with examples. Recent advancements such as integration of the AGF method with other tools (such as density functional theory and Boltzmann transport equation solvers) and extension of the AGF method to include anharmonicity are also presented. Comparisons of results from the AGF method to experimental measurements for superlattice and metal-graphene interfaces are provided.

KEY WORDS: *interfacial heat transfer, atomistic Green's function, phonon transport*

1. INTRODUCTION

The theoretical and experimental study of phonon transport across heterogeneous interfaces forms an important part of contemporary literature on nanoscale thermal transport.[1] Miniaturization of device sizes to submicron length scales has led to systems with increased density of interfaces and boundaries. Detailed understanding of heat transfer across interfaces is critical to applications such as the design of thermal interface and thermoelectric materials. Thermal interface materials (TIM) are used to reduce the temperature drop across solid-solid interfaces in many applications such as the interface between a microprocessor and a heat sink[2] or the interface between a heat source and a thermoelectric

ISSN: 1049–0787; ISBN: 1–978–56700–295–9/14/$35.00 + $00.00

NOMENCLATURE

$\hbar$	reduced Planck's constant (Js)
$\mathbf{k}$	wave vector (m^{-1})
$\mathcal{G}$	interfacial thermal conductance ($\mathrm{W/m^2K}$)
$\mathcal{T}$	transmission function
A	spectral function matrix (s^2)
a	uncoupled spectral function matrix (s^2)
c	wave velocity in string (m/s)
D	density of states (s)
E	energy associated with degrees of freedom (J)
F	forcing function
$\mathcal{F}^{-1}$	inverse Fourier transform
f	harmonic force constant (N/m)
f^o_{BE}	Bose-Einstein distribution function
G	total Green's function matrix
g	uncoupled Green's function (i.e., the Green's function before connecting the device and contacts)
H	harmonic matrix (s^{-2})
I	identity matrix
i	unitary imaginary number
J	energy flux between vibrational degrees of freedom (W)
k	harmonic force constant between vibrational degrees of freedom (N/m)
L	differential operator
LDOS	local density of states (s)
l	bond length in a one-dimensional (1D) chain of atoms
M	atomic mass (kg)
p	phonon polarizatio
q	heat flux ($\mathrm{W/m^2}$)
R	number of degrees of freedom in the contact
S	column vector representing excitation of device due to phonon waves from the contacts
s	source term representing inflow of phonons into the contact
T	temperature (K)
t	time (s)
t_o	time at which impulse is applied
U	interatomic potential (J)
u	atomic displacement (m)
v_g	group velocity (m/s)
Z	acoustic impedance ($\mathrm{kg/m^2s}$)
0^+	positive infinitesimal number

Greek Symbols

Γ	a matrix defined for algebraic convenience that physically represents the escape rate of phonons from the device into the contacts
γ	polarization specific escape rate
ζ	point of application of impulse
θ	angle of incidence
$\theta(t)$	Heaviside function
Σ	self-energy matrix
τ	connection harmonic matrix between groups of atoms (s^{-2})
ϕ	column vector representing vibrational degrees of freedom
χ	column vector representing change in the original contact vector ϕ^c after the contact and device are connected
ψ	column vector representing vibrational degrees of freedom in the connected device
ω	angular frequency (s^{-1})

Subscripts and Superscripts

$*$	complex conjugate
$\dagger$	conjugate transpose
AMM	acoustic mismatch model
c	contact region

NOMENCLATURE (Continued)

D	atoms in the device region that are not connected to either contacts
d	device region, including LD, D, and RD
DMM	diffuse mismatch model
LC	atoms in the left contact that are connected with the device
LCB	bulk portion of left contact representing atoms in left contact that do not have any bonds with atoms in the device
LD	atoms in the device region that are connected with atoms in left contact
RC	atoms in the right contact that are connected with the device
RCB	bulk portion of right contact representing atoms in right contact that do not have any bonds with atoms in the device
RD	atoms in the device region that are connected with atoms in right contact

device.[3] The engineering of nano-structured thermoelectric materials such as superlattices[4] and nanowires[5] relies on interfacial phonon scattering to reduce the thermal conductivity and increase the figure of merit. Although the overall impact and final objective of interface design can vary depending on the application, a thorough understanding of the physics of interfacial phonon transport is critical for all such applications.

The development of predictive theoretical and computational models is expected to aid the design of interfaces for the foregoing applications. The last decade has also seen a rapid development in experimental techniques to probe phonon transport at the nanoscale. Schwab et al.[6] performed carefully controlled experiments at very low temperatures of the order of 0.8 K and measured the quantum of thermal conductance (predicted theoretically earlier by Rego and Kirezenow[7]) for phonon transport in a one-dimensional channel. Techniques such as the 3ω method[8] and time-domain thermoreflectance[9] have been extensively used to study thermal transport at the nanoscale. Reference 1 provides a comprehensive review of the various metrology techniques. Simulation models are important to interpret and understand the results from measurements of phonon transport. Computational models also elucidate the finer details of interface transport, such as phonon mode conversion and the spectral dependence of phonon transmission. Such details are difficult to measure directly in experiments and are generally buried within the overall resistance value that is obtained from a measurement. However such detailed information can aid the engineering of phonon transmission across interfaces.

Consider two materials 1 and 2 joined together to form an interface. The heat flux from material 1 to 2 is given by the following integral:

$$q_{1\to 2} = \frac{1}{8\pi^3} \sum_p \int_0^{2\pi} \int_0^{\pi/2} \int_0^{\infty} \hbar\omega v_{\mathrm{g}}(\omega) f^o_{\mathrm{BE}}(\omega, T_1) \mathcal{T}(\mathbf{k}) k^2 dk \sin\theta \cos\theta d\theta d\phi \tag{1}$$

where the integration of phonon energies is performed over all azimuthal angles ϕ, all angles of incidence θ, and over all phonon wave vectors k. $f^o_{\mathrm{BE}}(\omega, T)$ denotes the

Bose-Einstein distribution function, and $v_g(\omega)\cos\theta$ denotes component of group velocity normal to the interface. $\mathcal{T}(\mathbf{k})$ denotes the phonon transmission probability, and p represents the various phonon polarizations. A similar expression can be written for the heat flux from material 2 to 1. Using the principle of detailed balance and for small temperature differences across the interface, the following expression can be obtained for the interfacial thermal conductance:

$$\mathcal{G} = \frac{1}{8\pi^3}\sum_p \int_0^{2\pi}\int_0^{\pi/2}\int_0^{\infty} \hbar\omega v_g(\omega)\frac{\partial f^o_{\mathrm{BE}}(\omega,T)}{\partial T}\mathcal{T}(\mathbf{k})k^2 dk \sin\theta\cos\theta d\theta d\phi \tag{2}$$

Once the dispersion relation and the closely associated group velocity are known, the problem of determining the interfacial thermal conductance reduces to calculating the transmission function $\mathcal{T}(\mathbf{k})$ for different polarizations. This is the central problem in modeling interfacial phonon transport, and various theoretical and computational models have been proposed in the literature to compute the transmission function. The acoustic mismatch model[10] (AMM) was one of the earliest efforts in this direction, for which the transmission function is based on the assumption that phonons reflect and transmit across interfaces in a specular fashion similar to acoustic waves (Fig. 1). The specular assumption, combined with stress and displacement continuity conditions at the interface, can be used to obtain the following expression for the transmissivity:[10,11]

$$\mathcal{T}_{\mathrm{AMM}} = \frac{4Z_1Z_2\cos\theta_1\cos\theta_2}{(Z_1\cos\theta_2 + Z_2\cos\theta_1)^2} \tag{3}$$

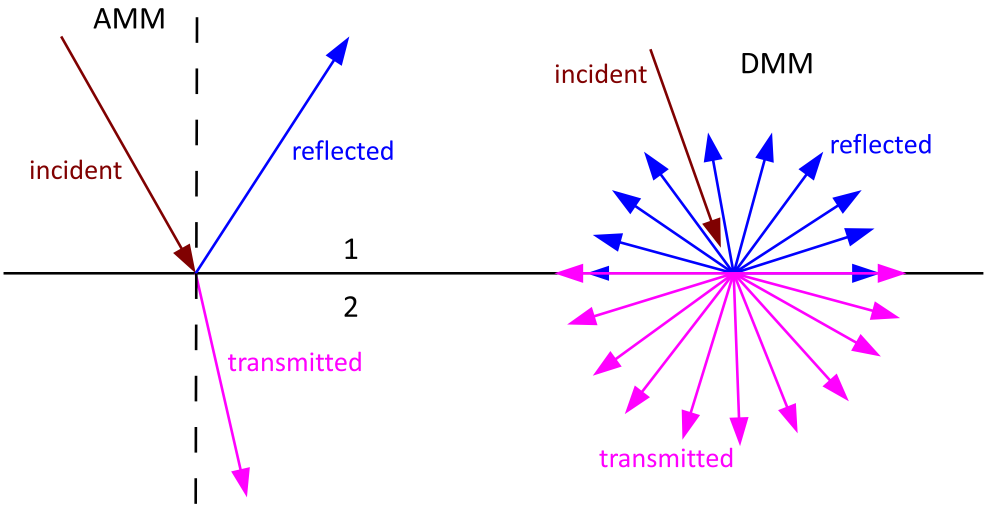

FIG. 1: Schematic of specular and diffuse scattering assumptions in the acoustic and diffuse mismatch models respectively. In the AMM, the reflected and transmitted waves have a definite angle determined from Snell's law. In the DMM, a uniform probability density exists for the directional distribution of reflected and transmitted waves.

where Z_1 and Z_2 denote the acoustic impedances of materials 1 and 2 and are defined as the product of mass density and acoustic wave velocity. θ_1 and θ_2 denote the angles of incidence and refraction, respectively, and are related through Snell's law of refraction. The transmissivity is independent of frequency and excludes the possibility of mode conversion at the interface. The assumption of specular reflection is valid only for perfectly smooth interfaces or for phonons with wavelengths much larger than the scale of interface roughness. Thus, the AMM is strictly valid only at low temperatures that are well below the Debye temperature, where the phonon distribution is concentrated in the long wavelength (acoustic) range. The AMM predicts a cubic dependence of thermal boundary conductance on temperature for three-dimensional (3D) materials.[10]

At high temperatures and in nonideal rough interfaces, phonon reflection and transmission at an interface are expected to be more diffuse than specular. Swartz and Pohl[12] performed measurements of thermal resistance at solid-solid interfaces for a range of temperatures from 1 to 300 K. Their experimental results matched well with the AMM predictions for temperatures up to 30 K, but the results diverged from theory for higher temperatures. This observation led them to consider the effects of diffuse interface scattering, and the diffuse mismatch model (DMM) was proposed.[11] The DMM assumes that the direction of phonon wave propagation after it reaches an interface is completely uncorrelated with its initial direction, i.e., a phonon forgets its identity after reaching the interface (Fig. 1). Under this assumption, the probability of transmission from material 1 to material 2 should be the same as the probability of reflection for a phonon from material 2 incident on the interface. The above argument combined with the principle of detailed balance leads to the following equation for the transmissivity:[11]

$$\mathcal{T}_{\text{DMM}}(\omega) = \frac{\sum\limits_{p_2} D_2(\omega) v_{\text{g}2}}{\sum\limits_{p_1} D_1(\omega) v_{\text{g}1} + \sum\limits_{p_2} D_2(\omega) v_{\text{g}2}} \tag{4}$$

where the summations are carried over different polarizations. Equation (4) assumes elastic scattering at the interface (i.e., a phonon from medium 1 of frequency ω can only transmit into a phonon of the same frequency ω irrespective of the mode). The DMM is more appropriate than the AMM at high temperatures where the phonon distribution is concentrated near the edge of the Brillouin zone and hence likely to be affected by surface roughness at the interface.

Extensions of both the AMM and DMM have been studied in the literature. A scattering-mediated AMM was proposed by Prasher and Phelan[13] where the effects of scattering near the interface were considered using an analogy with radiative transport. Prasher[14] also modified the AMM to account for weak van der Waals type bonding at the interface, because the traditional AMM assumes a perfectly welded contact. Duda et al.[15] considered different variations of the DMM where expressions for the transmissivity were obtained under various conditions that included partial to total diffuse scattering and elastic and inelastic scattering. Reddy et al.[16] performed calculations for thermal resistance by applying the DMM on the exact dispersion curve and showed that the resistance values could be significantly different from that obtained using the Debye model for dispersion.

In spite of the various extensions to the classical AMM and DMM, the central fact remains that neither of the traditional models explicitly accounts for phonon mode conversion at the interface. Also, neither considers the strength of bonding between materials that comprise the interface. Such bonding considerations are especially important[17] because the interface resistance is expected to be vastly different for a chemically bonded interface as compared to an interface that only involves weak physical interactions. As an example, the thermal interface resistance of palladium-bonded carbon nanotube arrays was found to be $\sim$50% less than the interface resistance of CNT arrays that were dry bonded (weak van der Waals interactions) to the substrate.[18] AMM and DMM also assume a perfect lattice for the materials that comprise the interface and do not consider the dependence of transmissivity on the detailed local arrangement of atoms. Such dependence is expected to be important especially at high temperatures for which transport is dominated by short-wavelength phonons.

In light of the above limitations, a need exists for atomistic interface transport models that explicitly consider the detailed atomic arrangement near the interface, the strength and nature of interfacial bonding. Molecular dynamics (MD), lattice dynamics (LD), and the atomistic Green's function (AGF) method are three popular atomistic techniques that have been used in the literature to calculate thermal interface resistance. MD is a direct method in the sense that all the computations are performed in the time domain, whereas LD and AGF are both frequency-domain techniques. All three methods require the definition of inter-atomic potentials, which if not known *a priori* should be derived from first principles calculations. The focus of this chapter is on the Green's function method, but here we also briefly describe MD and LD to highlight their important features.

Classical MD has emerged as a useful tool to study thermal transport across interfaces, especially with the emergence of enormous computational power in the last decade. The method primarily involves numerical integration of Newton's second law for every atom in the system. MD simulations can directly calculate total interface resistance without resorting to the Landauer approach and the transmission function formalism. However if spectral phonon transmission information is desired, carefully controlled MD simulations known as wave packet simulations must be employed.[19] Wave packet simulations typically involve a specific initial displacement pattern so as to excite a localized phonon wave of a particular polarization and frequency. This wave packet is allowed to propagate toward an interface, and the reflected and transmitted packets are analyzed to compute a mode-specific transmissivity.

An important feature of MD is the fact that anharmonic scattering is included in a very natural manner without any significant effort. Hence, MD is expected to be a useful tool at temperatures higher than the Debye temperature of the material, where anharmonic scattering is expected to significantly influence phonon transport. Another feature of MD is the fact that atomic positions near the interface need not be known *a priori* and can be relaxed during the simulation. However, standard molecular dynamics uses the classical Boltzmann distribution for phonon occupation statistics that is only valid at temperatures above the Debye temperature. At low temperatures, the quantum nature of the phonon occupation statistics is important and the Bose-Einstein distribution must to be employed. The classical nature of MD poses a serious limitation on its use for materials with a high Debye temperature; quantum corrections to the classical temperature should often be considered as discussed in Ref. 20. Results from MD simulations are also typically sensitive to domain size effects,[21] and hence a domain size study should always be performed.

Lattice dynamics (LD) is another useful atomistic method to compute thermal interface resistance. The method basically involves the substitution of plane-wave solutions for the incident, reflected, and transmitted waves at an interface; the amplitudes of the plane waves are solved by using the boundary conditions or equations of motion for atoms near the interface. We refer the reader to the Refs. 22–24 for the exact details involved in a LD calculation of thermal interface resistance. Unlike MD, LD is strictly valid only at low temperatures because of the use of harmonic force constants to describe the interactions between atoms. LD is appropriate at temperatures well below the Debye temperature, where anharmonic interface scattering can be neglected. Unlike MD, LD is a frequency-domain method and hence ideally suited for studying phonon mode and frequency specific transmission across interfaces. It does not require any special techniques such as the use of wave packets in MD to compute the spectral phonon transmissivity. Also, LD typically works on periodic systems and does not suffer from finite domain size effects.

The Green's function method is another atomistic technique to study electron and phonon transport across interfaces. The AGF technique for phonon transport was pioneered by Mingo and Yang,[25] where the method was used to study phonon transport in nanowires with an amorphous coating. The underlying phonon physics considered in the AGF approach is very similar to LD because both methods neglect anharmonic phonon processes. Although the AGF technique can be generalized to include anharmonic phonon interactions,[26] this extension requires significantly more effort than the basic harmonic formulation. Consequently most studies in the literature[25,27,28] have used the AGF equations with harmonic assumptions, and this approach will also be the primary focus of this chapter.

Similar to LD, the AGF method is suitable at low temperatures where the quantum phonon population distribution is important and anharmonic scattering is negligible. However as shown Section 2, the AGF formulation considers the LD equations of the system as a whole and obtains transmission equations that are applicable to any generalized geometrical configuration. Given any system, the AGF method requires only the computation of certain matrices (explained in more detail in Section 2) to compute the transmission coefficients. Hence, we need not worry about the details of the geometry and interface boundary conditions that would normally be required in a LD calculation. Also, the Green's function of the system can directly be used to obtain the local and global density of states (DOS) of a system; the procedure to obtain the DOS is not as straightforward in other methods.

In this review, our objective is to elucidate the fundamental concepts involved in the Green's function method for phonon transport and also to review some recent and advanced developments in the field. We first introduce the basic mathematical formulation in Section 2, and in Section 3 we discuss some computational issues involved in the numerical implementation. Sections 2 and 3 are both somewhat introductory in nature and are intended to appeal to readers with no prior knowledge of the Green's function technique. In Section 4, we review recent developments of the AGF technique, such as the inclusion of anharmonic scattering and the integration of AGF with ab initio methods, such as density functional theory (DFT). We also present some comparisons of results from AGF methods with experiments. Section 4 is intended for a more advanced reader seeking a comprehensive review of the contemporary literature on AGF. We then conclude the chapter with some future directions for research. A similar review that covers the fundamentals and some advanced concepts of AGF was written by Mingo.[29]

2. MATHEMATICAL FORMULATION

Our objective in this section is to derive the equations and matrices involved in the atomistic Green's function (AGF) method for phonon transport. As discussed Section 1, the AGF method considers the quantum phonon energy distribution and in its basic form is applicable at low temperatures. AGF has also been extended to include anharmonic scattering, which extends the range of applicable temperatures, making it a general method for studying nanoscale phonon transport. In spite of the rigorous nature of the method, its use is not very widespread among the engineering community, possibly due to the mathematical complexities of the technique. The Green's function technique for treating many-particle systems with interactions was first pioneered in the works of Martin and Schwinger[30] and Keldysh[31]. However, their formulations involved advanced concepts such as many-body perturbation theory with which engineers are not generally familiar. Datta[32–34] pioneered the formulation of the non-equilibrium Green's function (NEGF) method for electron transport using simpler ideas, the essence of which is to decouple the mechanics of transport from the entropy-generating scattering processes. Transport in a nanoscale device is usually ballistic with all the scattering processes concentrated only in the contacts (i.e., the two processes are spatially separated). Such an approach of decoupling processes that are traditionally intertwined has enabled wider adoption of the NEGF method in the engineering community.

In a similar spirit, we derive here the AGF equations for phonon transport.[32] Before embarking into the atomistic transport equations, we first solve a well-studied problem of acoustic wave transmission through strings using the concept of Green's functions. We believe that a continuum wave transmission problem would appeal directly to an engineer's intuition and help the readers understand the basic idea of a Green's function in order to better appreciate the atomistic counterpart that will be considered in the latter part of this section.

2.1 Continuum Green's Functions: An Example

A Green's function is a useful mathematical tool to solve non-homogeneous differential equations, such as the following steady, one-dimensional equation:

$$Lu(x) = F(x) \tag{5}$$

where L is a differential operator and F is a forcing function. The Green's function of a system is defined as the system's impulse response (i.e., the Green's function is the output from the system when driven with an impulse input)

$$LG(x;\zeta) = \delta(x-\zeta) \tag{6}$$

The impulse response $G(x;\zeta)$ can then be used to obtain the system's response $u(x)$ under an arbitrary excitation $F(x)$

$$u(x) = \int G(x,\zeta)F(\zeta)d\zeta \tag{7}$$

In this section, we derive the Green's function for acoustic wave propagation in a one-dimensional string and also obtain the classical AMM result for energy transmission across an interface. Here, we consider the problem of acoustic wave transmission across an interface between two strings made of different materials joined at $x = 0$ (Fig. 2). The wave speeds in the two strings are c_1 and c_2. A transverse acoustic wave is generated in one of the strings (say left) due to an impulse excitation at position $x = \zeta(< 0)$ and time $t = t_o$. According to the definition above, the solution $G_1(x,t;\zeta,t_o)$ for $x < 0$ gives the Green's function of the left string. Let the solution in the right string be $G_2(x,t;\zeta,t_o)$.

$$\begin{aligned} \frac{\partial^2 G_1}{\partial x^2} - \frac{1}{{c_1}^2}\frac{\partial^2 G_1}{\partial t^2} &= \delta(x-\zeta)\delta(t-t_o) \qquad \text{for } x < 0 \\ \frac{\partial^2 G_2}{\partial x^2} - \frac{1}{{c_2}^2}\frac{\partial^2 G_2}{\partial t^2} &= 0 \qquad \text{for } x > 0 \end{aligned} \tag{8}$$

Applying a Fourier transform on both the equations, we find

$$\begin{aligned} \frac{\partial^2 G_1}{\partial x^2} + \frac{\omega^2}{{c_1}^2}G_1 &= \delta(x-\zeta)e^{-i\omega t_o} \qquad \text{for } x < 0 \\ \frac{\partial^2 G_2}{\partial x^2} + \frac{\omega^2}{{c_2}^2}G_2 &= 0 \qquad \text{for } x > 0 \end{aligned} \tag{9}$$

The two fundamental solutions to the homogeneous wave equation are given by $\exp(i\omega x/c)$ and $\exp(-i\omega x/c)$. We use these fundamental solutions to write the solutions of Eq. (9) in the following form:

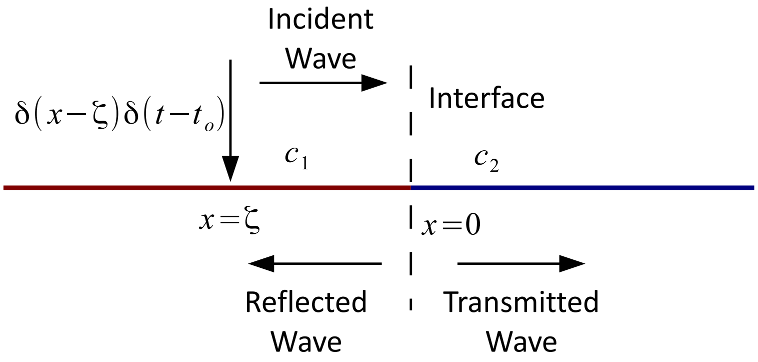

FIG. 2: Schematic of acoustic wave transmission across an interface between two strings with an impulse excitation at $x = \zeta$, $t = t_o$.

$$G_1 = \begin{cases} A_1 \exp\left(\dfrac{i\omega x}{c_1}\right) + B_1 \exp\left(\dfrac{-i\omega x}{c_1}\right) & \text{for } x < \zeta \\ C_1 \exp\left(\dfrac{i\omega x}{c_1}\right) + D_1 \exp\left(\dfrac{-i\omega x}{c_1}\right) & \text{for } \zeta < x < 0 \end{cases} \tag{10}$$

$$G_2 = A_2 \exp\left(\frac{i\omega x}{c_2}\right) + B_2 \exp\left(\frac{-i\omega x}{c_2}\right) \tag{11}$$

The interface continuity conditions at $x = 0$, the Green's function continuity condition at $x = \zeta$, and the discontinuity in first derivative of the Green's function at $x = \zeta$ combine to produce a solution for the constants in Eqs. (10) and (11). The constants A_1 and B_2 are zero because the wave must be traveling to the left for $x < \zeta$, and the transmitted wave for $x > 0$ must be traveling to the right. Solving for the constants, we obtain G_1 and G_2

$$\begin{aligned} G_1(x, \omega; \zeta, t_o) = {} & i\frac{c_1}{2\omega} \underbrace{\exp\left[i\omega\left(\frac{|x-\zeta|}{c_1} - t_o\right)\right]}_{\text{incident wave}} \\ & - i\frac{c_1}{2\omega} \underbrace{\left\{\frac{c_1 - c_2}{c_1 + c_2} \exp\left[-i\omega\left(\frac{x+\zeta}{c_1} + t_o\right)\right]\right\}}_{\text{reflected wave}} \end{aligned} \tag{12}$$

$$G_2(x, \omega; \zeta, t_o) = i\frac{c_1}{2\omega} \underbrace{\left\{\frac{2c_2}{c_1 + c_2} \exp\left[i\omega\left(\frac{x}{c_2} - \frac{\zeta}{c_1} - t_o\right)\right]\right\}}_{\text{transmitted wave}} \tag{13}$$

Equations (12) and (13) clearly identify the incident, reflected, and transmitted waves. The transmittance can then be calculated from the following equation:

$$\mathcal{T} = 1 - \frac{|\text{reflected wave}|^2}{|\text{incident wave}|^2} = 1 - \left(\frac{c_1 - c_2}{c_1 + c_2}\right)^2 = \frac{4c_1 c_2}{(c_1 + c_2)^2} \tag{14}$$

where $|\text{incident wave}|$ and $|\text{reflected wave}|$ denote amplitudes of incident and reflected waves, respectively. The energy transmission coefficient is dependent on the square of these amplitudes. The expression for the transmission coefficient above matches the classical AMM result in Eq. (3) for normal incidence. This can be seen by noting that the acoustic impedance in a 1D string can be defined as $Z = \sqrt{T\mu}$, where T is the tension in the string and μ is the mass per unit length. The wave velocity c is given by $c = \sqrt{T/\mu}$. In this section, we have interpreted the Green's function as the impulse response of a system and found the Green's function for a continuum wave transmission problem. We proceed to derive the Green's function method for atomistic phonon transport and show that the Green's function in the discrete atomistic case can also be interpreted as the impulse response of the system.

2.2 Atomistic Green's Function Method: Formulation

The AGF method is ideally suited for a geometry such as that shown in Fig. 3, where a small "device" region is connected to large reservoirs or "contacts" that are held at constant temperatures. The objective is to compute the spectral transmissivity for phonon transport from contact 1 to 2 so that it can be substituted in Eq. (2) to obtain the interface thermal conductance. The derivations in this section assume that the device is small enough that phonon transport can be considered to be ballistic or coherent. All phase-breaking scattering processes are assumed to be concentrated at the interfaces between the device and contacts. This assumption is not however a fundamental limitation of the Green's function method; more advanced formulations[26] include anharmonic scattering within the device and will be reviewed in Section 4. However, most current literature on AGF considers only harmonic interface and boundary scattering.

2.2.1 Harmonic Matrices

The AGF method is founded on the harmonic matrices of the contacts and device. The elements of the harmonic matrix physically represent the harmonic force constants of the bonds connecting various atoms. Mathematically, the harmonic matrix is defined as follows:

$$H = \{H_{pq}\} = \frac{1}{\sqrt{M_p M_q}} \begin{cases} \dfrac{\partial^2 U}{\partial u_p \partial u_q} & \text{if } p \neq q \\ -\displaystyle\sum_{k \neq q} \dfrac{\partial^2 U}{\partial u_q \partial u_k} & \text{if } p = q \end{cases} \tag{15}$$

where U is the interatomic potential energy function and u is the individual spatial displacement away from the equilibrium bond separation. The harmonic matrix is typically obtained by assuming a suitable form of interatomic potentials and then linearizing it to

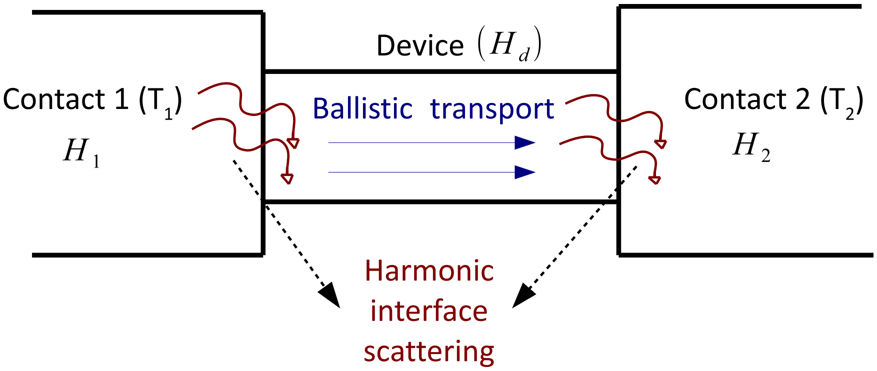

FIG. 3: Schematic of a typical phonon transport problem considered in the AGF formulation. All phase breaking processes occur due to harmonic interface scattering and ballistic phonon transport occurs in the device region. H_1, H_2 and H_d denote the harmonic matrices of isolated contacts and device, respectively.

obtain the harmonic force constants. The force constants can also be obtained from a first-principles DFT calculation as discussed further in Section 4. The foregoing model includes only harmonic springlike potentials; other more complex potentials that arise, for example, from Coulombic interactions in ionic materials could be included but are neglected in the present work. Given the harmonic matrix H of a closed system, the following eigenvalue equation is satisfied:

$$[\omega^2 I - H]\phi = 0 \tag{16}$$

where $\{\phi_p\} = u_p\sqrt{M_p}$ is the vector of atomic displacements multiplied by the square root of the corresponding atomic mass. However, in our problem the reservoirs or contacts are held at a constant temperature by an external heat source or sink (i.e., there is an exchange of phonons from the contacts to the surroundings). For such an open system, Eq. (16) requires modification to the following:[32]

$$[(\omega^2 + i0^+)I - H]\phi = s \tag{17}$$

where 0^+ is a small positive infinitesimal factor that introduces damping in the open system. It physically represents the leakage of phonons out of the contact. The fact that the term $i0^+$ introduces damping can be seen by considering a simple system with a single eigenfrequency ω_o. For such a system, the harmonic matrix H is just a number ω_o^2. The inverse Fourier transform of the term $\omega^2\phi$ becomes $-(d^2\phi/dt^2)$, and Eq. (16) in the time domain can be written as follows:

$$\frac{d^2\phi}{dt^2} = -\omega_o^2\phi \tag{18}$$

whose solution is given by $\phi = \exp(-i\omega_o t)$. Similarly, when Eq. (17) is written in the time domain, the solution is given by $\phi = \exp\left(i\sqrt{\omega_o^2 - i0^+}t\right) \approx \exp\left(-i\omega_o t\right)$ $\exp[-0^+t/(2\omega_o)]$, which represents a damped harmonic solution. Although the magnitude of this damping given by $i0^+$ may seem negligible, the overall effect is to produce a finite damping as this infinitesimal effect is applied over a semi-infinite region of the reservoir, and the product of infinitesimal and semi-infinite factors produce a finite effect. The source term s in Eq. (17) physically represents the inflow of phonons into the contact. The discussion below does not explicitly require calculation of s, which is eventually eliminated from the equations.

2.2.2 Green's Function Formulation

When the contacts and the device are coupled together, we need to use the total harmonic matrix H_{tot}

$$H_{\text{tot}} = \begin{bmatrix} H_1 & \tau_1^\dagger & 0 \\ \tau_1 & H_d & \tau_2 \\ 0 & \tau_2^\dagger & H_2 \end{bmatrix} \tag{19}$$

where H_1, H_2, and H_d represent the harmonic matrices of isolated contacts and the device, respectively. τ_1 and τ_2 are connection matrices that contain the force constants for bonds between atoms in the device and contacts. If the device and reservoir regions (both left and right) contain d and R degrees of freedom, respectively, then the matrices H_d and H_1 (or H_2) are of sizes $d \times d$ and $R \times R$, respectively. The matrix τ_1 (or τ_2) is of size $d \times R$. The reader that is not familiar with this idea of splitting the total harmonic matrix into its various components is referred to Section 3, where we consider a simple 1D atom chain example. Using the total harmonic matrix in Eq. (19), Eq. (17) for the entire system of device and contacts can be written as follows:[35]

$$\begin{bmatrix} (\omega^2 + i0^+)I - H_1 & -\tau_1^\dagger & 0 \\ -\tau_1 & \omega^2 I - H_d & -\tau_2 \\ 0 & -\tau_2^\dagger & (\omega^2 + i0^+)I - H_2 \end{bmatrix} \begin{Bmatrix} \phi_1^c + \chi_1 \\ \psi \\ \phi_2^c + \chi_2 \end{Bmatrix} = \begin{Bmatrix} s_1 \\ 0 \\ s_2 \end{Bmatrix} \quad (20)$$

where ϕ_1^c and ϕ_2^c are the eigenvectors of the isolated contacts, i.e., they satisfy the equations $[(\omega^2+i0^+)I-H_1]\phi_1^c = s_1$ and $[(\omega^2+i0^+)I-H_2]\phi_2^c = s_2$. $\chi_{1,2}$ represents change in the atomic displacements of the contacts after coupling with the device, and ψ represents the excitation of atoms in the device due to phonon waves from the contacts. Equation (20) is the same as Eq. (17) for the entire system of device and contacts. Considering the first row in Eq. (20), we obtain

$$\underbrace{[(\omega^2 + i0^+)I - H_1]\phi_1^c}_{s_1} + [(\omega^2 + i0^+)I - H_1]\chi_1 - \tau_1^\dagger\psi = s_1 \quad (21)$$

From Eq. (21), $\chi_1 = g_1\tau_1^\dagger\psi$ where $g_1 = [(\omega^2 + i0^+)I - H_1]^{-1}$ is the uncoupled Green's function of contact 1. Similarly by considering the third row of Eq. (20), it can be shown that $\chi_2 = g_2\tau_2^\dagger\psi$, where $g_2 = [(\omega^2 + i0^+)I - H_2]^{-1}$ is the uncoupled Green's function of the right contact. Substituting for $\chi_{1,2}$ into the device subset of equations [row 2 in Eq. (20)], the following equation for the device displacement vector ψ is obtained:

$$\{\psi\} = [\omega^2 I - H_d - \Sigma_1 - \Sigma_2]^{-1}\{S\} \quad (22)$$

where $G_d = [\omega^2 I - H_d - \Sigma_1 - \Sigma_2]^{-1}$ is the device subset of the overall Green's function. Σ_1 and Σ_2 are the self-energy matrices associated with contacts 1 and 2, defined by

$$\Sigma_1 = \tau_1 g_1 \tau_1^\dagger \quad \Sigma_2 = \tau_2 g_2 \tau_2^\dagger \quad (23)$$

The term S defined Eq. (24) physically represents the excitation of the device by phonon waves from the contacts

$$\{S\} = \underbrace{\tau_1\phi_1^c}_{S_1} + \underbrace{\tau_2\phi_2^c}_{S_2} \quad (24)$$

We emphasize here the distinction between the various Green's function matrices G_d and g_1, g_2. g_1 and g_2 are the Green's functions of the respective contacts calculated using the harmonic matrices H_1 and H_2. g_1 and g_2 have been referred to as bulk Green's function[36] or uncoupled Green's function[32,37] in prior literature. Such nomenclature arises from the fact that they are calculated using submatrices H_1 and H_2 that correspond to the bulk contacts in the total harmonic matrix. Green's functions calculated using specific submatrices of the total harmonic matrix are denoted by g_i throughout this chapter where the subscript corresponds to the region to which the uncoupled Green's function corresponds. Overall Green's functions are denoted by G with subscripts to denote specific subsets of the overall Green's function. For instance, G_d is the device subset of the overall Green's function of the system G_{tot} [i.e., G_{tot} is the Green's function obtained by using the harmonic matrix of the entire system (device + contacts)]. G_d is just a submatrix of G_{tot} corresponding to the device portion

$$G_{tot} = \begin{bmatrix} \omega^2 + i0^+ - H_1 & -\tau_1^\dagger & 0 \\ -\tau_1 & \omega^2 + i0^+ - H_d & -\tau_2 \\ 0 & -\tau_2^\dagger & \omega^2 + i0^+ - H_2 \end{bmatrix}^{-1} \tag{25}$$

The physical meaning of the self-energy is discussed in detail by Datta.[32,34] An important difference between $[H]$ and $[\Sigma]$ is that $[\Sigma]$ is not a Hermitian matrix, unlike $[H]$ which is guaranteed to be Hermitian and can hence have only real eigenvalues. In fact, the anti-Hermitian part of Σ defined by $\Gamma = i[\Sigma - \Sigma^\dagger]$ gives the phonons in the device a finite lifetime. Σ is similar to the infinitesimal $i0^+$ introduced in Eq. (17), and its magnitude is proportional to the rate of leakage of phonons from the device into the contacts. However, Σ is in general finite, unlike the infinitesimal damping 0^+ that we considered for the semi-infinite contacts. In the notation of Ref. 32, Γ is called the "escape rate" for phonons leaking from the device into the contacts. One of the advantages of the AGF formulation is its avoidance of explicit treatment of the large harmonic matrices associated with the contacts. Often we are interested only in the device region, and inspection of Eq. (22) reveals that the device displacements only depend on the device subset of the Green's function that can be computed without evaluating all the elements of G_{tot}. The details of efficient methods to compute a small subset of the overall Green's function will be discussed further in Section 3.

2.2.3 Density of States and Spectral Function

For a system with a harmonic matrix H ($n \times n$ matrix), the square root of the eigenvalues of H denoted by $\{\omega_1, \omega_2 \dots \omega_n\}$ give the discrete eigenfrequencies of the system. The global vibrational DOS of the system $D(\omega)$ (measured in seconds) is then given by

$$D(\omega) = \sum_{k=1}^{n} \delta(\omega - \omega_k) \tag{26}$$

The global DOS can also be defined in a slighly different form as follows

$$D(\omega) = \sum_{k=1}^{n} 2\omega\delta(\omega^2 - \omega_k^2) \tag{27}$$

Note that both Eqs. (26) and (27) are equivalent definitions of DOS and satisfy the following property:

$$\int_{\omega_k-}^{\omega_k+} \delta(\omega - \omega_k)d\omega = \int_{\omega_k-}^{\omega_k+} 2\omega\delta(\omega^2 - \omega_k^2)d\omega = 1 \tag{28}$$

However, defining the DOS in the form of Eq. (27) helps us relate the DOS directly to the Green's function defined in Section 2.2.2.

Equation (27) provides only the global DOS and does not provide information about the spatial variation of the DOS. The spatial variation of the DOS can be obtained by weighting each term in Eq. (27) with the corresponding phonon eigenvector. This method of obtaining the local phonon DOS is in direct analogy with the electronic local DOS defined in Ref. 32, where each term in the summation is weighted by the modulus squared of the corresponding electronic wave function. For phonons, the expression becomes

$$D(\vec{r};\omega) = \sum_{k=1}^{n} 2\omega\delta(\omega^2 - \omega_k^2)\phi_k(\vec{r})\phi_k^*(\vec{r}) \tag{29}$$

where ϕ_k denotes the eigenvector corresponding to eigenvalue ω_k^2. Equation (29) is not limited to the contacts alone and applies to any closed system whose eigenvalues ω_k^2 and eigenvectors ϕ_k satisfy the eigenvalue equation $\left[\omega_k^2 I - H\right]\phi_k = 0$. For a system with N atoms at positions $\vec{r}_1, \vec{r}_2 \ldots \vec{r}_n$, $\phi_k(\vec{r}_m)$ denotes the mth component of the phonon eigenvector corresponding to eigenvalue ω_k^2. Equation (29) can be interpreted as the diagonal elements of the matrix $D(\vec{r},\vec{r'};\omega)$ defined as follows:

$$D(\vec{r},\vec{r'};\omega) = 2\omega\sum_{k=1}^{n} \delta(\omega^2 - \omega_k^2)\phi_k(\vec{r})\phi_k^*(\vec{r'}) \tag{30}$$

Now we introduce the spectral function $A(\vec{r},\vec{r'};\omega)$ defined by

$$A(\vec{r},\vec{r'};\omega) = 2\pi\sum_{k=1}^{n} \delta(\omega^2 - \omega_k^2)\phi_k(\vec{r})\phi_k^*(\vec{r'}) \tag{31}$$

From Eqs. (30) and (31), the spectral function and the local DOS matrix are related by[35]

$$D(\vec{r},\vec{r'};\omega) = \frac{\omega A(\vec{r},\vec{r'};\omega)}{\pi} \tag{32}$$

Thus, the spectral function at a particular frequency is directly proportional to the DOS. The factor 2π in Eq. (31) is a numerical convenience that is useful when we approximate the delta function by a Lorentzian. The spectral function $A(\vec{r},\vec{r'})$ defined in Eq. (31) can be viewed as the real-space representation of the following generalized equation:[32]

$$A(\omega) = 2\pi\delta(\omega^2[I] - [H]) \tag{33}$$

Equation (31) emerges when Eq. (33) is evaluated in the real-space representation. When evaluating a function of a matrix (delta function in the present case), the matrix should first be diagonalized and the function is then evaluated for each of the diagonal elements of the matrix. This diagonal matrix is then transformable back to any particular basis. If we choose the eigenvectors of the matrix $[H]$ as the basis, then the spectral function becomes a diagonal matrix as $[H]$ is itself a diagonal matrix with its eigenvalues $\{\omega_1^2, \ldots, \omega_n^2\}$ along the diagonal. If the eigenvectors of $[H]$ are chosen as the basis, then the spectral function is given by the following diagonal matrix:

$$A(\omega) = 2\pi \begin{pmatrix} \delta(\omega^2 - \omega_1^2) & 0 & 0 & \ldots & 0 \\ 0 & \delta(\omega^2 - \omega_2^2) & 0 & \ldots & 0 \\ \vdots & & & \ddots & \vdots \\ 0 & \ldots & & 0 & \delta(\omega^2 - \omega_n^2) \end{pmatrix} \tag{34}$$

The trace (sum of diagonal elements) of the spectral function is proportional to the global DOS and is the same irrespective of the basis in which A is represented.

We can also express the spectral function $A(\omega)$ in terms of the Green's function of the system. This relation can be obtained by approximating the delta function as Lorentzian in the limit, where the width of the Lorentzian tends to zero.[32] In the eigenvector basis, the matrix $A(\omega)$ is diagonal as shown in Eq. (34). The kth diagonal element can be expressed in the following form using the Lorentzian function:

$$\begin{aligned} A(k, k; \omega) = 2\pi\delta(\omega^2 - \omega_k^2) &= \lim_{\eta \to 0^+} \frac{2\eta}{(\omega^2 - \omega_k^2)^2 + \eta^2} \\ &\approx i \left(\frac{1}{\omega^2 - \omega_k^2 + i0^+} - \frac{1}{\omega^2 - \omega_k^2 - i0^+} \right) \\ &= i[G(k, k; \omega) - G(k, k; \omega)^*] \end{aligned} \tag{35}$$

where the last equality $G(k, k; \omega) = 1/(\omega^2 - \omega_k^2 + i0^+)$ is obtained by evaluating the Green's function matrix $G(\omega) = [(\omega^2 + i0^+)I - H]^{-1}$ in the basis of eigenvectors of H. In such a basis where both $A(\omega)$ and $G(\omega)$ are diagonal matrices, the equation $A(k, k) = i[G(k, k) - G(k, k)^*]$ can be extended to the corresponding matrix form

$$\begin{aligned} A(\omega) = 2\pi\delta(\omega^2[I] - [H]) &= i\{[(\omega^2 + i0^+)I - H]^{-1} - [(\omega^2 - i0^+)I - H]^{-1}\} \\ &= i(G - G^\dagger) \end{aligned} \tag{36}$$

where

$$G(\omega) = [(\omega^2 + i0^+)I - H]^{-1} \tag{37}$$

is the total Green's function of the system as discussed in Section 2.2.2. Because we have convinced ourselves that the relation $A = i(G - G^\dagger)$ is valid in one particular basis in which the matrices are diagonal, the relation should be valid in any other basis as well. The fact that we can calculate quantities such as the local and global DOS directly from the Green's function is one of the advantages of using the AGF approach for interface transport as compared to lattice dynamics.

2.2.4 Green's Function: Physical Interpretation

In order to appreciate why $G(\omega)$ given by Eq. (37) is called the "Green's function," we first transform it to the time domain. In the basis of eigenvectors of $[H]$, $G(\omega)$ is a diagonal matrix and its inverse Fourier transform is just the inverse transform of its diagonal elements. Thus, the kth diagonal element of $G(t)$ is given by the following equation:

$$\begin{aligned} G(k,k;t) &= \mathcal{F}^{-1}[G(k,k;\omega)] = \mathcal{F}^{-1}\left(\frac{1}{\omega^2 + i0^+ - \omega_k^2}\right) \\ &= \frac{i}{2z}[\exp(-izt)\theta(-t) + \exp(izt)\theta(t)] \end{aligned} \tag{38}$$

where $\theta(t)$ is the Heaviside step function, $\mathcal{F}^{-1}$ denotes the inverse Fourier transform, and $z = \sqrt{\omega_k^2 - i0^+}$. It can be shown by simple substitution that $G(k,k;t)$ satisfies the following differential equation:

$$\left(\frac{\partial^2}{\partial t^2} + \omega_k^2 - i0^+\right) G(k,k;t) = -\delta(t) \tag{39}$$

More generally, the matrix $G(t)$ satisfies the following impulse response equation:

$$\left(-\frac{\partial^2}{\partial t^2} - [H] + i0^+\right) G(t) = \delta(t)[I] \tag{40}$$

Thus, the Green's function in the discrete atomistic case can also be interpreted physically as the impulse response of the lattice dynamics equations, similar to the Green's functions in the continuum problem discussed in Section 2.1.

2.2.5 Transmission Function

As mentioned in Section 1, the transmission probability of phonons is the only unknown quantity when calculating the interface thermal conductance using Eq. (2). In this section, we derive the spectral transmission function in terms of the Green's function and other matrices defined earlier. The formulation for the heat current is similar to that followed in Ref. 25, and the transmission function is expressed in terms of Green's functions using a similar methodology to that of Ref. 32. The energy E_p associated with the pth degree of freedom is given by:

$$E_p = \underbrace{\frac{1}{4}\sum_q (u_p^* k_{pq} u_q + u_q^* k_{qp} u_p)}_{\text{potential energy}} + \underbrace{\frac{1}{2} M_p \dot{u}_p^* \dot{u}_p}_{\text{kinetic energy}} \tag{41}$$

where k_{pq} represents the force constant between the pth and qth degree of freedom

$$k_{pq} = H_{pq}\sqrt{M_p M_q} \tag{42}$$

The time derivative of E_p is given by

$$\dot{E}_p = \frac{1}{4}\sum_q \left(\dot{u}_p^* k_{pq} u_q + u_p^* k_{pq} \dot{u}_q + \dot{u}_q^* k_{qp} u_p + u_q^* k_{qp} \dot{u}_p\right) + \frac{M_p}{2}\left(\ddot{u}_p^* \dot{u}_p + \dot{u}_p^* \ddot{u}_p\right) \tag{43}$$

From Newton's second law, $M_p \ddot{u}_p = -\sum_q k_{pq} u_q$ and $M_p \ddot{u}_p^* = -\sum_q k_{qp} u_q^*$. Using these equations, Eq. (43) can be reduced to

$$\dot{E}_p = \frac{1}{4}\sum_q \left(u_p^* k_{pq} \dot{u}_q + \dot{u}_q^* k_{qp} u_p - \dot{u}_p^* k_{pq} u_q - u_q^* k_{qp} \dot{u}_p\right) \tag{44}$$

Substituting $u_p = \phi_p \exp(-i\omega t)/\sqrt{M_p}$ and $u_q = \phi_q \exp(-i\omega t)/\sqrt{M_q}$, Eq. (44) simplifies to the following:

$$\dot{E}_p = \frac{\omega}{2i}\sum_q \left[\phi_p^* H_{pq} \phi_q - \phi_q^* H_{qp} \phi_p\right] = \sum_q J_{pq} \tag{45}$$

From Eq. (45), the energy flux between two degrees of freedom u_p and u_q is naturally defined by

$$J_{pq} = \frac{\omega}{2i}\left[\phi_p^* H_{pq} \phi_q - \phi_q^* H_{qp} \phi_p\right] \tag{46}$$

The total energy flux from the left contact to the device is obtained by summing Eq. (46) over all pairs of degrees of freedom in the contact and device and can be expressed as:

$$J_1 = \frac{\omega \operatorname{Tr}\left[\psi^\dagger \tau_1 \phi_1 - \phi_1^\dagger \tau_1^\dagger \psi\right]}{2i} \tag{47}$$

where the matrix τ_1 is the connection matrix between the degrees of freedom of the left contact and the device. The contact displacement vector ϕ_1 was previously expressed as a sum of the eigenvector of the isolated contact ϕ_1^c and a reflected wave χ_1. Substituting $\phi_1 = \phi_1^c + \chi_1$ into Eq. (47), we can separate the net energy flux into two parts

$$J_1 = \underbrace{\frac{\omega \operatorname{Tr}\left[\psi^\dagger \tau_1 \phi_1^c - \phi_1^{c\dagger} \tau_1^\dagger \psi\right]}{2i}}_{\text{Inflow}(J_{1,i})} - \underbrace{\frac{\omega \operatorname{Tr}\left[\chi_1^\dagger \tau_1^\dagger \psi - \psi^\dagger \tau_1 \chi_1\right]}{2i}}_{\text{Outflow}(J_{1,o})} \tag{48}$$

In Eq. (48), the term containing the uncoupled eigenvector of the contact ϕ_1^c is interpreted as an inflow term and the term containing χ_1, the induced displacement vector in the contact after connecting to the device is interpreted as the outflow term. We first focus on the inflow term here. From Eqs. (22) and (24), we know that $\psi = G_d S = G_d(S_1 + S_2)$ and $S_1 = \tau_1 \phi_1^c$. Substituting in the inflow term of Eq. (48)

$$J_{1,i} = \frac{\omega \operatorname{Tr}\left[S^\dagger G_d^\dagger S_1 - S_1^\dagger G_d S\right]}{2i} \tag{49}$$

The source terms from the two contacts add incoherently to produce the net heat flux, and there exists no definite phase relation between the sources from the contacts. Therefore,

$$S_1^\dagger S_2 = S_2^\dagger S_1 = 0 \tag{50}$$

Using Eq. (50) and remembering that the trace is independent of the order of multiplication, Eq. (49) can be simplified as follows:

$$\begin{aligned} J_{1,i} &= \frac{\omega \operatorname{Tr}\left[S_1 S_1^\dagger G_d^\dagger - S_1 S_1^\dagger G_d\right]}{2i} \\ &= \frac{\omega \operatorname{Tr}\left[S_1 S_1^\dagger A_d\right]}{2} \end{aligned} \tag{51}$$

where we have used the relation $A_d = i(G_d - G_d^\dagger)$ to obtain the second equality. A_d denotes the device subset of the overall spectral function. To obtain the total inflow, we need to sum Eq. (51) over the source terms contributed by the different eigenvectors of the left contact:

$$\begin{aligned} J_{1,i} &= \frac{1}{2}\sum_k \omega_k \operatorname{Tr}\left(\tau_1 \phi_{1k}^c \phi_{1k}^{c\dagger} \tau_1^\dagger A_d\right) \\ &= \frac{1}{2}\operatorname{Tr}\left[\tau_1 \left(\sum_k \omega_k \phi_{1k}^c \phi_{1k}^{c\dagger}\right) \tau_1^\dagger A_d\right] \end{aligned} \tag{52}$$

where the summation extends over all the eigenvectors of the left contact. To express Eq. (52) in terms of Green's functions, we need to consider the following normalization condition for phonons in the contact. The idea is to equate the classical energy (kinetic + potential) to the quantum energy of phonon modes. Equation (41) gives the total energy associated with the pth degree of freedom. As before, from Newton's second law $\sum_q k_{pq} u_q = -M_p \ddot{u}_p$ and $\sum_q k_{qp} u_q^* = -M_p \ddot{u}_p^*$. Substituting into Eq. (41), we find for E_p

$$E_p = -\frac{1}{4}(M_p u_p^* \ddot{u}_p + M_p u_p \ddot{u}_p^*) + \frac{1}{2} M_p \dot{u}_p^* \dot{u}_p \tag{53}$$

The classical energy of the pth degree of freedom associated with a particular eigenfrequency ω_k is calculated by substituting $u_{p,k} = \phi_{p,k}^c \exp(-i\omega_k t)/\sqrt{M_p}$ into Eq. (53)

$$E_p = \omega_k^2 |\phi_{p,k}^c|^2 \tag{54}$$

where $\phi_{p,k}^c$ denotes the pth component of the kth eigenvector with eigenvalue ω_k^2. The classical energy of the pth degree of freedom over a frequency square range of $(\omega^2, \omega^2 + d\omega^2)$ is given by

$$E_p(\omega^2) = \sum_{\omega_k^2 \in (\omega^2, \omega^2 + d\omega^2)} \omega_k^2 |\phi_{p,k}^c|^2 \tag{55}$$

The quantum energy of phonon modes in the frequency square range $(\omega^2, \omega^2 + d\omega^2)$, associated with the pth degree of freedom is given by

$$\begin{aligned} E_p(\omega^2) &= \hbar\omega D(\vec{r}_p, \omega^2) f^o_{\text{BE}}(\omega, T_1) d\omega^2 \\ &= \hbar\omega \frac{a_1(p,p;\omega^2)}{2\pi} f^o_{\text{BE}}(\omega, T_1) d\omega^2 \end{aligned} \tag{56}$$

where $D(\vec{r}_p, \omega^2)$ denotes the local density of states associated with the pth degree of freedom. We have used the fact that local density of states at the pth degree of freedom is given by the pth diagonal component of the spectral function of isolated contact a_1. Similar to the uncoupled Green's functions, we denote the uncoupled spectral function by a. Equating the classical [Eq. (55)] and quantum [Eq. (56)] energies and extending the respective equations to their corresponding matrix forms

$$\sum_{\omega_k^2 \in (\omega^2, \omega^2 + d\omega^2)} \omega_k \phi_k^c \phi_k^{c\dagger} = \hbar \frac{a_1}{2\pi} f^o_{\text{BE}}(\omega, T_1) d\omega^2 \tag{57}$$

Thus,

$$\sum_{\text{all } k} \omega_k \phi_k^c \phi_k^{c\dagger} = \int_0^\infty \frac{\hbar}{2\pi} a_1 f^o_{\text{BE}}(\omega, T_1) d(\omega^2) \tag{58}$$

Substituting the above expression into Eq. (52) gives the rate of energy inflow as follws:

$$J_{1,i} = \int_0^\infty \frac{\hbar\omega}{2\pi} \operatorname{Tr}(\tau_1 a_1 \tau_1^\dagger A_d) f^o_{\text{BE}}(\omega, T_1) d\omega \tag{59}$$

$$= \int_0^\infty \frac{\hbar\omega}{2\pi} \operatorname{Tr}(\Gamma_1 A_d) f^o_{\text{BE}}(\omega, T_1) d\omega \tag{60}$$

where $\Gamma_1 = i[\Sigma_1 - \Sigma_1^\dagger] = i[\tau_1(g_1 - g_1^\dagger)\tau_1^\dagger] = \tau_1 a_1 \tau_1^\dagger$ is the "escape rate" for the connection between the left contact and the device.

We next consider the outflow term in Eq. (48). Substituting $\chi_1 = g_1 \tau_1^\dagger \psi$ into the outflow term, we find

$$\begin{aligned} J_{1,o} &= \frac{\omega \operatorname{Tr}[\psi^\dagger \tau_1 g_1^\dagger \tau_1^\dagger \psi - \psi^\dagger \tau_1 g_1 \tau_1^\dagger \psi]}{2i} \\ &= \frac{\omega \operatorname{Tr}[\psi^\dagger \tau_1 a_1 \tau_1^\dagger \psi]}{2} && (a_1 = i(g_1 - g_1^\dagger)) \\ &= \frac{\omega \operatorname{Tr}[\psi^\dagger \Gamma_1 \psi]}{2} && (\Gamma_1 = \tau_1 a_1 \tau_1^\dagger) \\ &= \frac{\omega \operatorname{Tr}[G_d S S^\dagger G_d^\dagger \Gamma_1]}{2} && (\psi = G_d S) \\ &= \frac{\omega \operatorname{Tr}[G_d(S_1 S_1^\dagger + S_2 S_2^\dagger) G_d^\dagger \Gamma_1]}{2} && (S_1^\dagger S_2 = S_2^\dagger S_1 = 0) \end{aligned} \tag{61}$$

Similar to the inflow term, we sum over all the source terms contributed by the eigenvectors of the left and right contacts

$$
\begin{aligned}
J_{1,o} &= \frac{1}{2}\,\mathrm{Tr}\left[G_d\left(\sum_j \omega_{1,j} S_{1,j} S_{1,j}^{\dagger} + \sum_k \omega_{2,k} S_{2,k} S_{2,k}^{\dagger}\right) G_d^{\dagger}\Gamma_1\right] \qquad (62)\\
&= \frac{1}{2}\,\mathrm{Tr}\left\{G_d\left[\tau_1\left(\sum_j \omega_{1,j}\phi_{1,j}\phi_{1,j}^{\dagger}\right)\tau_1^{\dagger} + \tau_2\left(\sum_k \omega_{2,k}\phi_{2,k}\phi_{2,k}^{\dagger}\right)\tau_2^{\dagger}\right] G_d^{\dagger}\Gamma_1\right\}
\end{aligned}
$$

where the summations over j and k extend over all the eigenvectors of the left and right contacts, respectively. Equation (62) can be simplified using the normalization condition in Eq. (58) and can be written as follows:

$$
J_{1,o} = \int_0^{\infty} \frac{\hbar\omega}{2\pi}\,\mathrm{Tr}\{G_d[f_{\mathrm{BE}}^{o}(\omega, T_1)\Gamma_1 + f_{\mathrm{BE}}^{o}(\omega, T_2)\Gamma_2]G_d^{\dagger}\Gamma_1\}d\omega \qquad (63)
$$

Equation (64) (proven in Ref. 32) further simplifies the outflow term

$$
A_d = G_d\Gamma G_d^{\dagger} = \underbrace{G_d\Gamma_1 G_d^{\dagger}}_{A_1} + \underbrace{G_d\Gamma_2 G_d^{\dagger}}_{A_2} \qquad (64)
$$

where A_1 and A_2 are components corresponding to contributions from the left and right contacts, respectively. Substituting Eq. (64) into Eq. (63), the outflow term becomes

$$
J_{1,o} = \int_0^{\infty} \frac{\hbar\omega}{2\pi}\,\mathrm{Tr}[f_{\mathrm{BE}}^{o}(\omega, T_1)A_1\Gamma_1 + f_{\mathrm{BE}}^{o}(\omega, T_2)A_2\Gamma_1]d\omega \qquad (65)
$$

The net heat flow from the left contact to the device is therefore given by

$$
\begin{aligned}
J_1 &= J_{1,i} - J_{1,o}\\
&= \int_0^{\infty} \frac{\hbar\omega}{2\pi}\,\mathrm{Tr}[f_{\mathrm{BE}}^{o}(\omega, T_1)\Gamma_1 A_d - f_{\mathrm{BE}}^{o}(\omega, T_1)\Gamma_1 A_1 - f_{\mathrm{BE}}^{o}(\omega, T_2)\Gamma_1 A_2]d\omega\\
&= \int_0^{\infty} \frac{\hbar\omega}{2\pi}\,\mathrm{Tr}[\Gamma_1 A_2][f_{\mathrm{BE}}^{o}(\omega, T_1) - f_{\mathrm{BE}}^{o}(\omega, T_2)]d\omega \qquad (A_d = A_1 + A_2)\\
&= \int_0^{\infty} \frac{\hbar\omega}{2\pi}\,\mathrm{Tr}[\Gamma_1 G_d\Gamma_2 G_d^{\dagger}][f_{\mathrm{BE}}^{o}(\omega, T_1) - f_{\mathrm{BE}}^{o}(\omega, T_2)]d\omega \qquad (66)
\end{aligned}
$$

At steady state, this energy flux must also equal the net flux from the device to the right contact and therefore, Eq. (66) gives the net heat flow from the left to the right contact. For small temperature differences, we can approximate the difference in the distribution functions using a Taylor series expansion to obtain interface thermal conductance

$$\mathcal{G} = \int_{0}^{\infty} \frac{\hbar\omega}{2\pi} \underbrace{\mathrm{Tr}[\Gamma_1 G_d \Gamma_2 G_d^{\dagger}]}_{\mathcal{T}(\omega)} \frac{\partial f_{\mathrm{BE}}^{o}}{\partial T} d\omega \tag{67}$$

where the transmissivity $\mathcal{T}(\omega) = \mathrm{Tr}[\Gamma_1 G_d \Gamma_2 G_d^{\dagger}]$.

3. 1D ATOM CHAIN AND COMPUTATIONAL DETAILS

Our objective in this section is to illustrate how the equations derived above are implemented in practice. We study a simple 1D atom chain example and calculate the various matrices, such as H_d, $\tau_{1,2}$, $g_{1,2}$, $\Sigma_{1,2}$, and G, analytically. In the process, we also discuss a few computational subtleties that are necessary to understand when implementing the AGF method on a computer. These are related to the choice of the infinitesimal 0^+ and efficient numerical techniques to calculate the Green's function. The 1D atom chain example considered here is simple enough to write analytical expressions, but at the same time it serves to illustrate computational details that are relevant to the multi-dimensional transport problem as well.

Consider a 1D atomic chain (Fig. 4) with three device atoms connected to semi-infinite left and right contacts. We use a nearest-neighbor model for the interaction between atoms. The total harmonic matrix for the entire system (device + contact) is given by [see Eq. (19)]

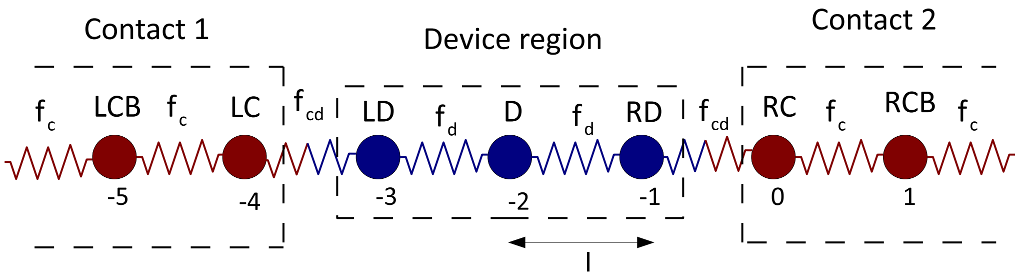

FIG. 4: Schematic of a 1D atom chain with three device atoms connected to semi-infinite contacts on either side. Numbers below the atoms denote the respective atom indices. f_d represents the spring constant for connections between device atoms, f_c represents the spring constant for connection between contact atoms, and f_{cd} represents the connection between device and contact atoms. l denotes the spacing between atoms and for simplicity is assumed to be the same for device and contact atoms. The mass of the contact atoms is m_c and that of device atoms is m_d.

$$H_{\text{tot}} = \begin{array}{c} \begin{array}{ccccccc} \phi_{-5} & \phi_{-4} & \phi_{-3} & \phi_{-2} & \phi_{-1} & \phi_{0} & \phi_{1} \end{array} \\ \left(\begin{array}{ccccccc} \ddots & & & & & & \\ \frac{-f_c}{m_c} & \frac{f_c+f_{cd}}{m_c} & \frac{-f_{cd}}{\sqrt{m_c m_d}} & & [0] & & \\ & \frac{-f_{cd}}{\sqrt{m_c m_d}} & \frac{f_d+f_{cd}}{m_d} & \frac{-f_d}{m_d} & & & \\ & & \frac{-f_d}{m_d} & \frac{2f_d}{m_d} & \frac{-f_d}{m_d} & & \\ & [0] & & \frac{-f_d}{m_d} & \frac{f_d+f_{cd}}{m_d} & \frac{-f_{cd}}{\sqrt{m_c m_d}} & \\ & & & & \frac{-f_{cd}}{\sqrt{m_c m_d}} & \frac{f_c+f_{cd}}{m_c} & \frac{-f_c}{m_c} \\ & & & & & & \ddots \end{array} \right) \end{array} \tag{68}$$

The total harmonic matrix can be written in the form of Eq. (19), where the submatrices are defined as follows:

$$H_1 = \begin{pmatrix} & \ddots & & & \\ [0] & -\frac{f_c}{m_c} & \frac{2f_c}{m_c} & -\frac{f_c}{m_c} & 0 \\ & [0] & -\frac{f_c}{m_c} & \frac{2f_c}{m_c} & -\frac{f_c}{m_c} \\ & & [0] & -\frac{f_c}{m_c} & \frac{f_c+f_{cd}}{m_c} \end{pmatrix}$$

$$H_2 = \begin{pmatrix} \frac{f_c+f_{cd}}{m_c} & -\frac{f_c}{m_c} & [0] & & \\ -\frac{f_c}{m_c} & \frac{2f_c}{m_c} & -\frac{f_c}{m_c} & [0] & \\ 0 & -\frac{f_c}{m_c} & \frac{2f_c}{m_c} & -\frac{f_c}{m_c} & [0] \\ & & & \ddots & \end{pmatrix} \tag{69}$$

$$H_d = \begin{pmatrix} \frac{f_d+f_{cd}}{m_d} & -\frac{f_d}{m_d} & 0 \\ -\frac{f_d}{m_d} & \frac{2f_d}{m_d} & -\frac{f_d}{m_d} \\ 0 & -\frac{f_d}{m_d} & \frac{f_d+f_{cd}}{m_d} \end{pmatrix}$$

$$\tau_1 = \underbrace{\begin{pmatrix} \ldots & [0] & \ldots & -\dfrac{f_{cd}}{\sqrt{m_c m_d}} \\ \ldots & [0] & \ldots & 0 \\ \ldots & [0] & \ldots & 0 \end{pmatrix}}_{R \text{ columns}} \quad \tau_2 = \underbrace{\begin{pmatrix} 0 & \ldots & [0] & \ldots \\ 0 & \ldots & [0] & \ldots \\ -\dfrac{f_{cd}}{\sqrt{m_c m_d}} & \ldots & [0] & \ldots \end{pmatrix}}_{R \text{ columns}} \tag{70}$$

Here, H_1 and H_2 are large matrices of size $R \times R$. τ_1 and τ_2 are of size $3 \times R$, since the number of device degrees of freedom is 3. We showed in Section 2 that the device portion of the Green's function can be written in the form $G_d = [\omega^2 I - H_d - \Sigma_1 - \Sigma_2]^{-1} = [\omega^2 I - H_d - \tau_1 g_1 \tau_1^\dagger - \tau_2 g_2 \tau_2^\dagger]^{-1}$. To proceed further we need to compute Σ_1 and Σ_2, which in turn requires us to compute the uncoupled Green's functions (g_1, g_2) of the respective contacts.

3.1 Computing Uncoupled Contact Green's Function

Although the connection matrices are large, Eq. (70) indicates that both τ_1 and τ_2 have only one nonzero element, because only one atom of the device is connected to one atom of the respective contacts. Also, to compute the Green's function G we only need to compute the product $\tau_{1,2} g_{1,2} \tau_{1,2}^\dagger$ instead of g_1 and g_2 explicitly. Because τ_1 and τ_2 have only one nonzero element, we only need to compute the last diagonal element of g_1 or the first diagonal element of g_2. The remaining elements in g_1 and g_2 are not necessary because they do not contribute to the product $\tau_1 g_1 \tau_1^\dagger$ or $\tau_2 g_2 \tau_2^\dagger$. $g_1(R, R)$ and $g_2(1, 1)$ correspond to the contact atoms that bond with the device. This is shown schematically in Fig. 4 where the contact atoms are split into two categories: LCB (RCB) and LC (RC). The atoms in LCB (RCB) correspond to the bulk of the contact and do not have any bonds with device atoms. Only the atoms in LC (RC) have bonds with device atoms in the region LCD (RCD). The atoms in region D correspond to interior atoms of the device that do not have any bonds with the contacts. On the basis of this notation, the harmonic matrices of the contacts can be further split into components corresponding to the regions LC (RC) and LCB (RCB)

$$H_1 = \begin{pmatrix} H_{\text{LCB}} & H_{\text{LCB,LC}}^\dagger \\ H_{\text{LCB,LC}} & H_{\text{LC}} \end{pmatrix} \tag{71}$$

where

$$H_{\text{LCB}} = \begin{pmatrix} \ddots & & \\ -\dfrac{f_c}{m_c} & 2\dfrac{f_c}{m_c} & -\dfrac{f_c}{m_c} \\ [0] & -\dfrac{f_c}{m_c} & 2\dfrac{f_c}{m_c} \end{pmatrix} \quad H_{\text{LCB,LC}} = \underbrace{\begin{pmatrix} 0 & \ldots & 0 & -\dfrac{f_c}{m_c} \end{pmatrix}}_{R-1 \text{ columns}}$$

$$H_{\text{LC}} = \left\{ \frac{f_{cd} + f_c}{m_c} \right\} \tag{72}$$

We need only the elements of the uncoupled Green's function that correspond to atoms in the region LC (RC). In general such elements of the uncoupled Green's function are called the surface Green's function. The self-energy matrices Σ_1 and Σ_2 can be redefined in terms of the surface Green's function as follows:

$$\begin{aligned}\Sigma_1 &= \tau_1 g_1 \tau_1^\dagger = \tau_{\mathrm{LC,LD}} g_{\mathrm{LC}} \tau_{\mathrm{LC,LD}}^\dagger \\ \Sigma_2 &= \tau_2 g_2 \tau_2^\dagger = \tau_{\mathrm{RC,RD}} g_{\mathrm{RC}} \tau_{\mathrm{RC,RD}}^\dagger \end{aligned} \tag{73}$$

where $\tau_{\mathrm{LC,LD}}$ and $\tau_{\mathrm{RC,RD}}$ are submatrices of τ_1 and τ_2. The remaining submatrices of τ_1 and τ_2 are just zero matrices. Because only a small portion of atoms near the surface of the contact bond with the device, the surface Green's function matrix is in general much smaller in size compared to the overall uncoupled Green's function matrix. In the present 1D atom chain example, the surface Green's function is merely a single element while the full uncoupled Green's function is a matrix of size $R \times R$, where R is typically a very large number. Next, we discuss a couple of approaches to compute the surface Green's function for the 1D atom chain example. The first technique gives an exact analytical expression for the surface Green's function. However, such analytical results can only be obtained for simple systems, such as the 1D atom chain, and iterative numerical techniques are required for more complicated systems. The decimation technique is a popular numerical technique to compute the surface Green's function, and we illustrate the basic ideas of the method using the 1D atom chain example.

3.1.1 Analytical Calculation of Surface Green's Function

Here, we describe a simple matrix inversion relation that is necessary to understand the present method. Consider a matrix

$$M = \begin{pmatrix} A & B \\ C & D \end{pmatrix} \tag{74}$$

where A, B, C, and D are submatrices. A specific subset of M^{-1}, say the portion corresponding to matrix D in the original matrix, can be computed using the following relation:

$$M^{-1} = \begin{pmatrix} \cdots & \cdots \\ \cdots & [D - CA^{-1}B]^{-1} \end{pmatrix} \tag{75}$$

The above relation can easily be verified by substitution and is discussed in Ref. 32 as well. Using Eq. (75), the surface Green's function in the present case is given by

$$\begin{aligned} g_1^s &= [\underbrace{(\omega^2 + i0^+)I - H_{\mathrm{LC}}}_{D} - \underbrace{H_{LCB,LC}}_{C} \underbrace{[(\omega^2 + i0^+)I - H_{\mathrm{LCB}}]^{-1}}_{A^{-1}} \underbrace{H_{\mathrm{LCB,LC}}^\dagger}_{B}]^{-1} \\ &= [(\omega^2 + i0^+)I - H_{\mathrm{LC}} - H_{\mathrm{LCB,LC}} g_{LCB} H_{\mathrm{LCB,LC}}^\dagger]^{-1} \end{aligned} \tag{76}$$

where $g_{\mathrm{LCB}} = [(\omega^2 + i0^+)I - H_{\mathrm{LCB}}]^{-1}$ is a large matrix of size $(R-1) \times (R-1)$. Once again, we note that $H_{\mathrm{LCB,LC}}$ has only one nonzero element and, therefore, only the last diagonal element of g_{LCB} requires evaluation. This can be thought of as the surface Green's function of the bulk portion of the left contact. But this time, we can exploit the homogeneity of the bulk contact to calculate the surface Green's function analytically. First, we assume that the bulk contact contains only $n-1$ layers and calculate the surface Green's function $g^s_{\mathrm{LCB},n-1}$. Now if the number of layers becomes n, then the surface Green's function is given by [using Eq. (75)]:

$$g^s_{\mathrm{LCB},n} = \frac{1}{\omega^2 + i0^+ - 2f_c/m_c - (f_c/m_c)(g^s_{\mathrm{LCB},n-1})(f_c/m_c)} \tag{77}$$

Now as $n \to \infty$, $g^s_{\mathrm{LCB},n} = g^s_{\mathrm{LCB},n-1} = g^s_{\mathrm{LCB}}$ and we obtain a quadratic equation for the surface Green's function g^s_{LCB} that can directly be solved to obtain the following analytical expression for g^s_{LCB}:

$$g^s_{\mathrm{LCB}} = \frac{-[2(f_c/m_c) - (\omega^2 + i0^+)] - \sqrt{[2(f_c/m_c) - (\omega^2 + i0^+)]^2 - 4(f_c/m_c)^2}}{2(f_c/m_c)^2} \tag{78}$$

Note that Eq. (78) gives only the surface Green's function of a bulk contact and must be substituted into Eq. (76) to obtain the surface Green's function of the contact. Equation (77) could also be considered an iterative equation that can be used to estimate $g^s_{\mathrm{LCB},n}$ from $g^s_{\mathrm{LCB},n-1}$, where the number of layers n is progressively increased until $|g^s_{\mathrm{LCB},n} - g^s_{\mathrm{LCB},n-1}|$ becomes smaller than a predefined tolerance. However, such a numerical technique is rarely used in practice because the number of layers considered increases in a linear fashion with the number of iterations (i.e., the number of layers considered in the contact is $n+1$ after n iterations). Convergence is expected to be slow for such a method. The decimation technique discussed below is a more efficient numerical method because the number of layers increases as an exponential function of the number of iterations (i.e., the number of contact layers considered after n iterations is 2^n).

3.1.2 Decimation Technique

Here, we describe the iterative decimation equations for computing surface Green's function of the right contact; the ideas can be extended for the left contact as well. This presentation is simply a specific form of the decimation technique applied to a 1D atom chain. The reader is referred to Ref. 38 for a more general formulation of the method. From the definition of the Green's function, we have

$$[(\omega^2 + i0^+)I - H_2][g_2] = [I] \tag{79}$$

where g_2 is the full uncoupled Green's function of the right contact and can be written in terms of the atom indices (see Fig. 4) as follows:

$$g_2 = \begin{pmatrix} g_{0,0} & g_{0,1} & \cdots & \cdots & \cdots \\ g_{1,0} & g_{1,1} & \cdots & \cdots & \cdots \\ \vdots & \vdots & \ddots & \cdots & \cdots \\ g_{n,0} & g_{n,1} & \cdots & g_{n,n} & \cdots \\ \vdots & \vdots & \vdots & \vdots & \ddots \end{pmatrix} \tag{80}$$

As discussed earlier in this section, we need only $g_{0,0}$, the first diagonal element of g_2. Using Eq. (69) for H_2 and expanding Eq. (79), we obtain the following set of equations:

$$\begin{aligned}
\left(\omega^2 + i0^+ - \frac{f_c + f_{cd}}{m_c}\right) g_{0,0} + \frac{f_c}{m_c} g_{1,0} &= 1 \\
\frac{f_c}{m_c} g_{0,0} + \left(\omega^2 + i0^+ - \frac{2f_c}{m_c}\right) g_{1,0} + \frac{f_c}{m_c} g_{2,0} &= 0 \\
\frac{f_c}{m_c} g_{1,0} + \left(\omega^2 + i0^+ - \frac{2f_c}{m_c}\right) g_{2,0} + \frac{f_c}{m_c} g_{3,0} &= 0 \\
\vdots &= \vdots \\
\frac{f_c}{m_c} g_{n-1,0} + \left(\omega^2 + i0^+ - \frac{2f_c}{m_c}\right) g_{n,0} + \frac{f_c}{m_c} g_{n+1,0} &= 0
\end{aligned} \tag{81}$$

where the equations are obtained by multiplying the corresponding row of $[(\omega^2 + i0^+)I - H_2]$ and the first column of g_2. The above set of equations can be written compactly in the following form:

$$H_0^s g_{0,0} + \tau_0 g_{1,0} = 1 \tag{82}$$

$$\tau_0 g_{m-1,0} + H_0^b g_{m,0} + \tau_0 g_{m+1,0} = 0 \qquad m = 1, 2, 3, \ldots \tag{83}$$

where H_0^s and H_0^b denote the surface and bulk harmonic force constants respectively at the zeroth iteration; τ_0 denotes the connection force constant between adjacent layers at the zeroth iteration.

$$H_0^s = \left(\omega^2 + i0^+ - \frac{f_c + f_{cd}}{m_c}\right) \quad H_0^b = \left(\omega^2 + i0^+ - \tfrac{2f_c}{m_c}\right) \quad \tau_0 = f_c \tag{84}$$

Now we eliminate $\{g_{1,0}, g_{3,0}, g_{5,0} \ldots\}$ from the equation set in Eq. (83). The equations for $\{g_{1,0}, g_{3,0}, g_{5,0} \ldots\}$ can be written compactly as follows:

$$g_{2m+1,0} = \frac{-\tau_0 g_{2m,0} - \tau_0 g_{2m+2,0}}{H_0^b} \qquad m = 0, 1, 2, \ldots \tag{85}$$

Substituting the above set of equations into Eqs. (82) and (83), we obtain the following set of equations in terms of $\{g_{0,0}, g_{2,0}, g_{4,0}, g_{6,0} \ldots\}$:

$$H_1^s g_{0,0} + \tau_1 g_{2,0} = 1 \tag{86}$$

$$\tau_1 g_{2m-2,0} + H_1^b g_{2m,0} + \tau_1 g_{2m+2,0} = 0 \qquad m = 1, 2, 3, \ldots \tag{87}$$

where H_1^s and H_1^b denote the effective surface and bulk force constants of the layers after the first iteration; τ_0 denotes the effective connection force constant between alternate layers

$$H_1^s = H_0^s - \frac{\tau_0^2}{H_0^b}, \quad H_1^b = H_0^b - 2\frac{\tau_0^2}{H_0^b}, \quad \tau_1 = -\frac{\tau_0^2}{H_0^b} \tag{88}$$

Observation of Eqs. (82) and (83) and Eqs. (86) and (87) reveal that both the equation sets have exactly the same form, albeit with different set of coefficients. Hence, the process of elimination can be continued in a similar manner repeatedly until convergence. For instance, we could eliminate $\{g_{2,0}, g_{6,0}, g_{10,0}, \ldots\}$ from Eq. (87) to obtain an equation set in terms of $\{g_{0,0}, g_{4,0}, g_{8,0}, \ldots\}$. After n such steps, we obtain the following:

$$H_n^s g_{0,0} + \tau_n g_{2^n,0} = 1 \tag{89}$$

$$\tau_n g_{(m-1)2^n,0} + H_1^b g_{m2^n,0} + \tau_1 g_{(m+1)2^n,0} = 0 \qquad m = 1, 2, 3, \ldots \tag{90}$$

where the new surface and bulk force constants are given by H_n^s and H_n^b, respectively, and τ_n denotes the effective connection between layers separated by 2^n units

$$H_n^s = H_{n-1}^s - \frac{\tau_{n-1}^2}{H_{n-1}^b}, \quad H_n^b = H_{n-1}^b - 2\frac{\tau_{n-1}^2}{H_{n-1}^b}, \quad \tau_n = -\frac{\tau_{n-1}^2}{H_{n-1}^b} \tag{91}$$

The key idea in the decimation technique is that $\tau_n \to 0$ as n becomes sufficiently large.[38] This is expected because τ_n describes the effective interaction between layers separated by 2^n units and such long-range interactions should tend to zero as n increases. If n is large enough such that $\tau_n \approx 0$, then from Eq. (89) we obtain the following equation for the surface Green's function $g_{0,0}$:

$$g_{0,0} = \frac{1}{H_n^s} \tag{92}$$

This also denotes the point after which the surface and bulk force constants do not change with further iterations. The above discussion forms the crux of the decimation technique. Note that for a general three-dimensional solid, the surface, bulk, and connection force constants are in general not numbers but matrices. But the essential ideas are similar to the example illustrated above. An exponential increase in the number of contact layers with the number of iterations is responsible for the fast convergence characteristics of the decimation technique.

3.2 Choice of 0^+

The contacts assumed in the AGF method are idealized semi-infinite systems with a continuous eigenspectrum. However, numerical computations are always performed on a finite system and a finite system has a discrete eigenspectrum with sharp variations in DOS. Such a system with sharp variations in DOS does not possess the essential characteristics of a good "contact" (see Section 8.4 in Ref. 32 for a detailed discussion). The complex infinitesimal $i0^+$ broadens the discrete spectrum into a continuous spectrum, thereby approximating the effect of a semi-infinite contact with the finite-sized contacts that are used in numerical computations. For a well-behaved contact, the exact value of 0^+ does not affect the results from the AGF calculation as long as the infinitesimal is chosen within an appropriate range. The factor 0^+ must be larger than the spacing between the discrete eigenfrequencies in the finite-sized contact so that sufficient broadening of the discrete levels is produced.

In order to demonstrate how the choice of the infinitesimal factor affects the AGF computations, we consider a 1D atom chain with $f_c = 25$ N/m, $f_d = 50$ N/m, $m_c = m_d = 20$ amu and $l = 5.5$ Å. For the 1D atom chain, the surface Green's function can be computed exactly by substituting the analytical solution from Eq. (78) into Eq. (76). In fact the infinitesimal factor 0^+ in the analytical solution can be set to zero as the analytical solution is exact for a semi-infinite contact and no need exists to introduce external broadening. Now we compare the surface Green's function computed using the decimation technique for different choices of the infinitesimal with the exact analytical solution. We assume that the infinitesimal takes the following functional form:

$$0^+(\omega) = \delta_o \omega^2 \tag{93}$$

where δ_o is a constant that is varied over an order of magnitude from 10^{-3} to 10^{-9}. Equation (93) is a heuristic choice of the infinitesimal factor consistent with prior literature.[35] The factor ω^2 is used to scale the infinitesimal with respect to the order of magnitude of eigenvalues of the harmonic matrix. Also, the factor δ_o could be chosen to be a function of frequency (see Refs. 25 and 35) so that the infinitesimal takes on larger or smaller values, depending on the density of singularities. Figure 5(a) shows a plot of the relative error in the surface Green's function computed from the decimation technique, as a function of frequency, for different values of δ_o. The surface Green's function more closely matches the analytical result as the value of δ_o is reduced. But this increased accuracy comes at the cost of increased computational time because the number of iterations required in the decimation technique also increases as δ_o is reduced [Fig. 5(b)]. This increased computational time is insignificant for the present 1D atom chain example; however, a trade-off between the accuracy of results and computational time would dictate the choice of the infinitesimal for AGF calculations on more complex interface configurations. A convergence study on the surface Green's function by reducing $0^+(\omega)$ is recommended.

Figure 6 shows the transmission function and LDOS at the center of the device using $\delta_o = 10^{-7}$. At low frequencies, the transmission function is 1 as long-wavelength phonons experience no interface scattering. Both the transmission function and the LDOS decay to zero at the cutoff frequency of the contact as $f_c < f_d$ for the present example. The transmission function also exhibits peaks and troughs that correspond to constructive and destructive interferences of phonon waves in the device region.[35]

4. ADVANCED TREATMENTS

This section is devoted to a review of contemporary literature on the AGF method. To date, most phonon AGF work has been largely based on the harmonic assumption.[25,27,35,36,39] The mathematical formulation provided in Section 2 forms the basis of most such work. In the first part of this section, we review some examples from the literature where the harmonic AGF formulation is used to compute phonon transmission across dimensionally

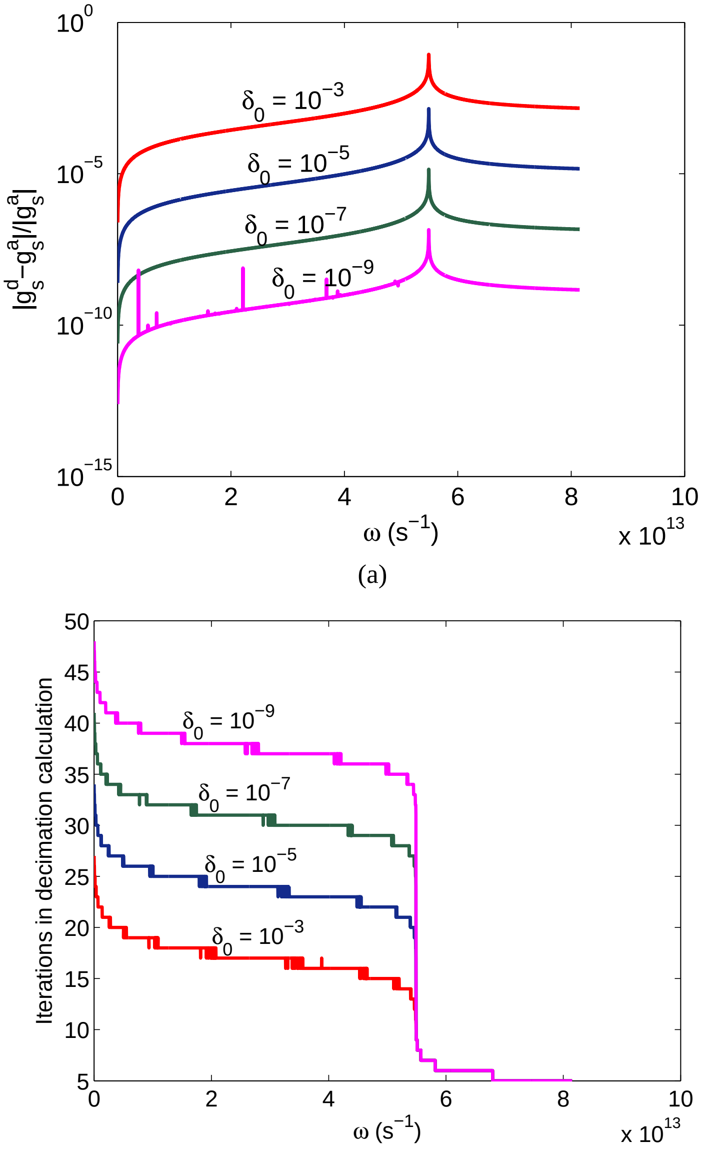

(a)

(b)

FIG. 5: (a) Relative difference between surface Green's function computed using the decimation technique and the analytical result. g_s^d and g_s^a denote the surface Green's functions from the decimation and analytical calculations respectively. (b) Number of iterations required in the decimation calculation for different values of the infinitesimal factor δ_o.

mismatched and bulk interfaces. We also present an extension of the formulation in Section 2 to compute polarization specific transmission functions. Recent work by Mingo[26] extended the AGF method to include anharmonic interactions and showed that such interactions can significantly influence phonon transport at an interface. We review the

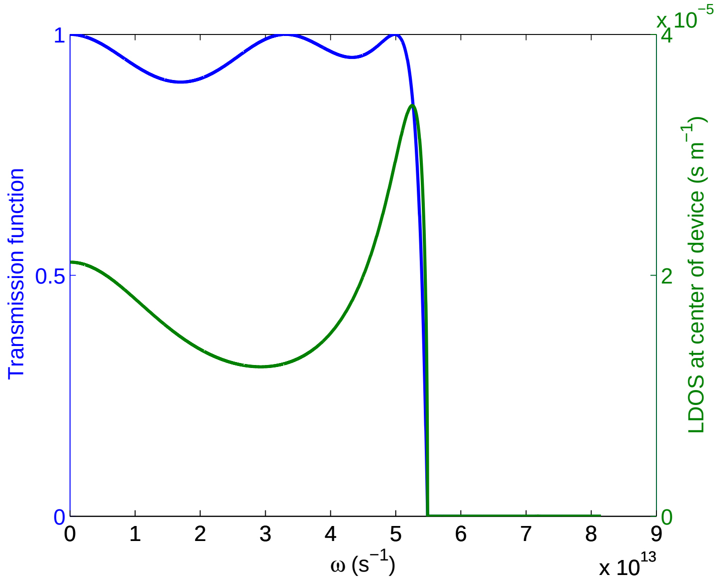

FIG. 6: Spectral transmission function and LDOS at the middle device atom.

underlying formulation behind the anharmonic extension of the AGF method in Section 4.2. A growing interest also exists in developing integrated solvers to address complex mesoscale phonon transport problems.[40] A few published papers[39,41,42] have demonstrated the feasibility of integrating the AGF technique with other computational methods. For instance, the first-principles based DFT (Refs. 43 and 44) can be used to provide inputs for the AGF method.[39,41] The AGF method can also provide interface transmission inputs to mesoscale techniques such as the Boltzmann transport equation (BTE). In the latter part of this section, we introduce some of these advanced treatments and review examples from the literature. We then conclude Section 4 with some comparisons of results from AGF methods with experiments.

4.1 Phonon Transport in Harmonic Systems

A number of studies have been published on the application of the harmonic AGF formulation to different materials of interest. As mentioned in Section 2, the harmonic assumption is justified when the device is small enough such that internal device scattering can be ignored. Mingo and Yang[25] studied phonon wave transport in nanowires with an amorphous coating. They developed the approach of using a full quantum mechanics based AGF method to solve ballistic or semiballistic phonon transport. Because of the dielectric property of nanowires, phonons are the dominant energy carrier, and electronic contributions to heat transfer were not considered. The paper used a self-consistent scheme to predict heat flux in the amorphous coating, which avoids full-field calculations of full dynamical matrices of the coating and the wire. The approach used to handle the amorphous coating can be extended and used in other amorphous coated systems as well. Zhang et al.[35] used a 1D atomic chain example to demonstrate the process involved in obtaining the phonon transmission function. In this section, we discuss application of the AGF method to a 1D harmonic system, a 1D device that is sandwiched between 2D contacts (denoted by a 2D-1D-2D interface), an interface between bulk materials, and also the procedure to obtain a polarization-specific transmission function. The overall approach involved in calculating transmission functions and thermal conductance in these problems is very similar to the foregoing exposition in the present work, but some details require further elaboration for complete understanding.

4.1.1 Phonon Transport in 1D Harmonic Systems

With the growing research interest in graphene and related materials, the AGF method has been adopted to study phonon transport across graphene nanoribbon[45,46] (GNR) and carbon nanotube[39] (CNT) interfaces. Huang et al.[45] investigated GNRs with small width mismatches between contacts and the device. A mismatched GNR-GNR interface is shown in Fig. 7. Here, the width of GNR is denoted by n (the number of graphene unit cells in the width direction) and the length of GNR is denoted by m (the number of graphene unit cells in the ribbon's axial direction). Figure 7 shows a GNR interface in which the contacts are both four-graphene-unit-cells wide, and the device is three-unit-cells wide and one-unit-cell long. This structure is denoted as "$4-3-4$ $m=1$." The first and last numbers represent the width of the contacts, and the middle number is the device width.

A fourth nearest-neighbor force constant (4NNFC) model is used to establish the matrices that describe interactions among carbon atoms. The process of establishing the dynamical equation is the same as that previously introduced with the 1D atom chain. Because the system is harmonic, the acoustic sum rule is enforced based on a simple scheme in which only diagonal elements of the dynamical matrix are corrected. In Fig. 8, the transmission function for the geometry in Fig. 7 is shown. Also shown are the transmission functions for pristine $n=3$ and $n=4$ AGNR ("A" denotes armchair configuration) cases.

The results reveal that at very low frequencies, the transmission is similar to that for pristine AGNR cases (red and black curves in Fig. 8) because low-frequency phonons can avoid interface scattering from the local discontinuity. The decreasing transmission function between highlighted points 1 and 2 (indicated by arrows in Fig. 8) reflects changes in phonon dispersion structure produced by the size mismatch. Transmission functions at several frequencies are circled to illustrate the effect. For example, at point 3, the transmission

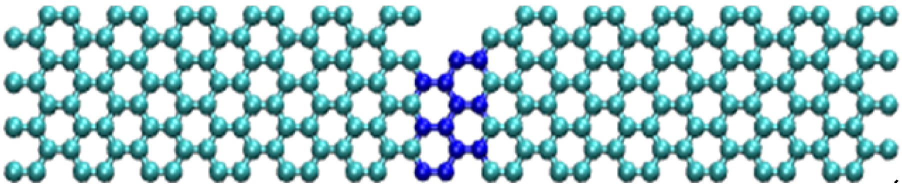

FIG. 7: Schematic view of a $4-3-4$ GNR structure with a device length of $m=1$. (Reprinted with permission from American Institute of Physics Publishing LLC, Copyright 2010).[45]

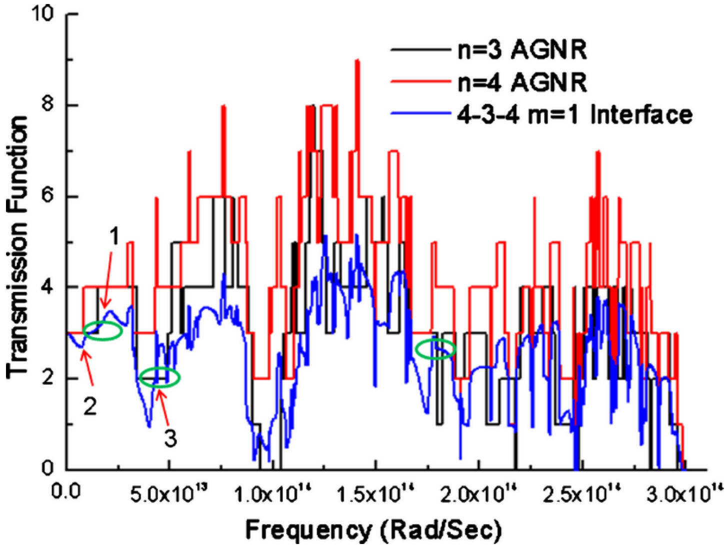

FIG. 8: Comparison of transmission functions between smooth and rough interfaces. (Reprinted with permission from American Institute of Physics Publishing LLC, Copyright 2010).[45]

function at the mismatch interface exhibits a peak similar to the spike on the $n = 4$ AGNR transmission function curve and is also higher than the transmission function for the $n = 3$ AGNR at that frequency. This occurs because the very short device length admits phonon modes that tend to match those of the contacts more closely than those of the device. Conversely, for longer devices, the overall phonon dynamics will be more affected by the device structure and the transmission function will be more influenced by the device.

Overall, the GNR cases can be solved in the same fashion as the 1D atom chain using the AGF method. However, the method that Zhang et al.[35] used to obtain the surface Green's function in the 1D atomic chain case is substituted by the decimation technique.[38]

4.1.2 Phonon Transport at 2D-1D-2D Interfaces

The AGF method can also be used to predict phonon transport at point contact interfaces. In such systems, the devices are low-dimensional confined nanostructures, such as GNRs, and the contacts are infinitely large in at least one dimension, such as graphene. The same notation (n, m) used earlier is used here to represent the size of the GNR. In a system such as graphene-GNR-graphene, each contact's unit cell must be defined differently from the 1D cases discussed earlier. The unit cell must include all atoms in the contacts that have interactions with the device. Figure 9 shows the unit cell of contacts (in red) in a graphene-AGNR-graphene case. One difference between 1D and 2D contacts, such as graphene, is the existence of parallel wavevectors in the contacts (k_y) that are used to represent phonon wave components in the parallel direction.

The uncoupled Green's function of contacts can be computed based on the assumption of no interactions between adjacent unit cells. Thus,

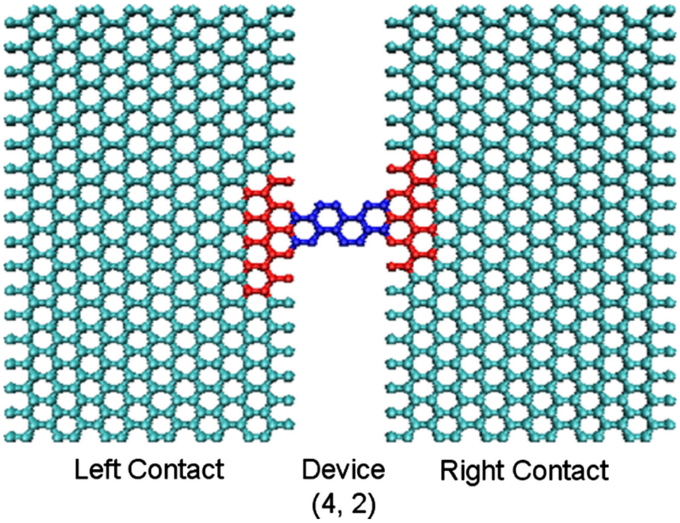

FIG. 9: A graphene-AGNR-graphene structure. (Reprinted with permission from American Institute of Physics Publishing LLC, Copyright 2010).[46]

$$g_{i,i}(\omega, \vec{k_y}) = \lim_{\delta \to 0} [(\omega^2 + \delta i)I - H_{i,i}(\vec{k_y})]^{-1} \tag{94}$$

where I is the identity matrix, the subscript i is the index for unit cells; g is the surface Green's function, and $H_{i,i}$ is the harmonic matrix of unit cell i. Also, note that both the Green's function and harmonic matrix are a function of $k_y \in (0, 2\pi/c)$, where c is the lattice constant in the parallel direction. After iteration, the Green's function of the contacts can be calculated from

$$g_m(\omega, \vec{k_y}) = [\omega^2 I - H_{m,m}(\vec{k_y}) - H_{m,m-1}(\vec{k_y}) g_{m-1}(\vec{k_y}) H_{m-1,m}(\vec{k_y})]^{-1} \tag{95}$$

where m is the index of the unit cell in the contact next to the device region and g_{m-1} is the Green's function of the unit cell one layer deep in the contacts and is determined by the decimation calculation. Comparison of Eq. (94) with Eq. (95) reveals that the perturbation δ in Eq. (94) has been substituted by a frequency and wave vector dependent matrix $H_{m,m-1}g_{m-1}H_{m-1,m}$, which serves as a correction to the dynamical system due to the bulk contact.

A mean contact Green's function is calculated by integrating over the k_y space to capture all phonon waves

$$\begin{aligned} g_{1(2)s}(\omega) &= \frac{1}{k_{y,\max}} \int g_{1(2)s}(\omega, k_y) dk_y \\ &= \frac{1}{k_{y,\max}} \sum_{k_y} g_{1(2)s}(\omega, k_y) \frac{k_{y,\max}}{N} \\ &= \frac{1}{N} \sum_{k_y} g_{1(2)s}(\omega, k_y) \end{aligned} \tag{96}$$

where N is the number of numerical integration cells in k_y space, 200 in this work. Self-energy matrices are obtained using the mean contact Green's function to include all phonon modes

$$\Sigma_{1(2)}(\omega) = \tau_{\mathrm{L(R)C,L(R)D}}g_{1(2)s}(\omega)\tau^{\dagger}_{\mathrm{L(R)C,L(R)D}} \tag{97}$$

The rest of the process involved in calculating phonon transmission function is essentially the same as that introduced in Section 2.

Here we summarize the differences in applying the AGF method on a 1D system and a 2D-1D-2D system. First, the unit cells of contacts include a group of atoms that is different from the atoms of a primitive unit cell. For instance, the primitive unit cell of graphene consists of two atoms. However, a much bigger unit cell is used in the 2D-1D-2D system (Fig. 9) to include all the atoms that interact with device. Second, the wave vector in the periodic y-direction is used to address the periodicity along the direction parallel to the interface. Third, the contact Green's function is a summation of the Green's functions of all possible wave vectors k_y to include all phonon modes. This summation is performed before the self-energy and device Green's function calculation. Phonon transport in 3D-1D-3D problem can be solved in a similar fashion, with an additional summation over k_x apart from k_y.[36]

The thermal conductances of graphene-GNR-graphene structures for a $(4, 2)$ armchair-GNR (AGNR) and a $(4, 2)$ Zigzag-GNR (ZGNR) as the device are shown in Fig. 10 as a function of temperature together with the conductances of homogeneous GNRs of the same device width. The conductances of both cases with dimensional mismatch are moderately reduced from the corresponding pristine GNR values. The results also reveal that the graphene-ZGNR-graphene structure produces significantly higher thermal conductance

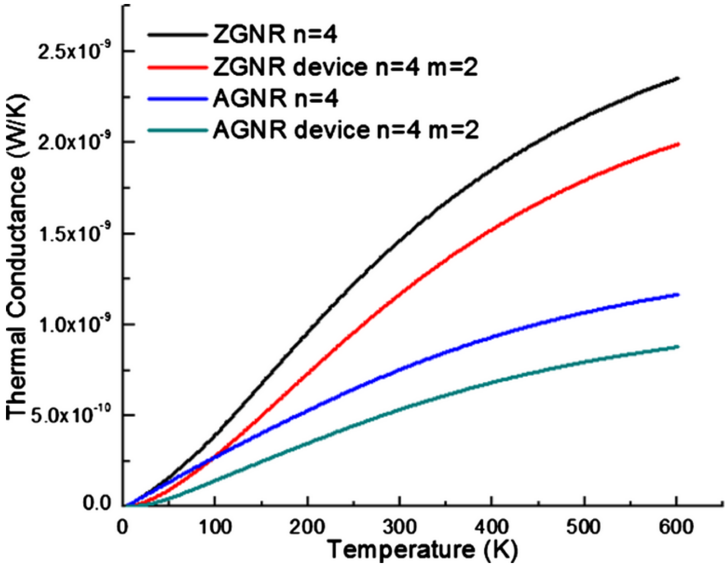

FIG. 10: Thermal conductances of abrupt confined junctions between graphene and GNR compared to the thermal conductance of free-standing GNRs. (Reprinted with permission from American Institute of Physics Publishing LLC, Copyright 2010).[46]

than the graphene-AGNR-graphene structure. This is because of the existence of more phonon modes and a wider frequency range of phonons in the ZGNR as compared to AGNR.

4.1.3 Phonon Transport Across Bulk Interfaces

Zhang et al.[27] considered an interface of Si/Ge and demonstrated the application of AGF method in a heterogeneous interface between two bulk materials. The direction perpendicular to interface is defined as z; the x and y directions are parallel to the interface plane. Because of translational invariance in the x-y plane (directions parallel to the interface), the transmission function is solved for each $\vec{k_{||}}$ independently, which is different from the systems discussed previously. To allow the decimation technique to be performed in the most efficient way, the Si lattice is stretched by 4% to match the lattice constant of Ge in the x-y plane. Otherwise, the unit cell on the Si side has to be defined to consist of 26 by 26 primitive unit cells and 25 by 25 primitive unit cells in the Ge side, so as to match unit cell size. The computational cost to solve phonon transport in such unit cells is very high. The stretching does not need to be performed on homogeneous interfaces if the lattice constants are the same between contacts and device (e.g., graphene-GNR interface). The change in force constants caused by stretching are estimated using the materials' Poisson's ratio.

The contact Green's functions can be calculated in the same fashion as shown in Eq. (95). The only difference is that the Green's function is not only a function of ω and k_y, but also k_x. The transmission function is dependent on $\vec{k_{||}}$ and is written as

$$\mathcal{T}(\vec{k_{||}}) = \mathrm{Tr}(\Gamma_1(\omega, \vec{k_{||}})G_d(\omega, \vec{k_{||}})\Gamma_2(\omega, \vec{k_{||}})G_d^{\dagger}(\omega, \vec{k_{||}})) \tag{98}$$

The total heat flux is written as an integral over phonon frequency ω and parallel wavevectors $\vec{k_{||}}$

$$\int_{\omega}\int_{\vec{k_{||}}} \frac{\hbar\omega}{2\pi}\mathcal{T}(\omega, \vec{k_{||}})(f_{\mathrm{BE}}^{o}(\omega, T_1) - f_{\mathrm{BE}}^{o}(\omega, T_2))\frac{d\vec{k_{||}}}{(2\pi)^2}d\omega \tag{99}$$

A comparison of thermal boundary resistance (TBR) of a Si/Ge interface obtained from AGF calculations and the predictions from AMM was made by Zhang et al.[27] and is shown in Fig. 11. At low temperatures, both methods predict a T^{-3} dependence of TBR because of the linear phonon dispersion. At temperatures of $<$20 K, the results from both methods agree well because the long wavelength phonons experience little boundary scattering.

4.1.4 Polarization-Specific Transmission Function

The transmission function is a summation over each phonon polarization's probability of transmission through an interface. The traditional AGF method cannot examine individual phonon polarization's transmissivity. An extension of the AGF methodology is developed by Huang et al.[47] to obtain polarization-specific transmission functions in an attempt to enable multiscale modeling. The development of the method is based on the orthogonal

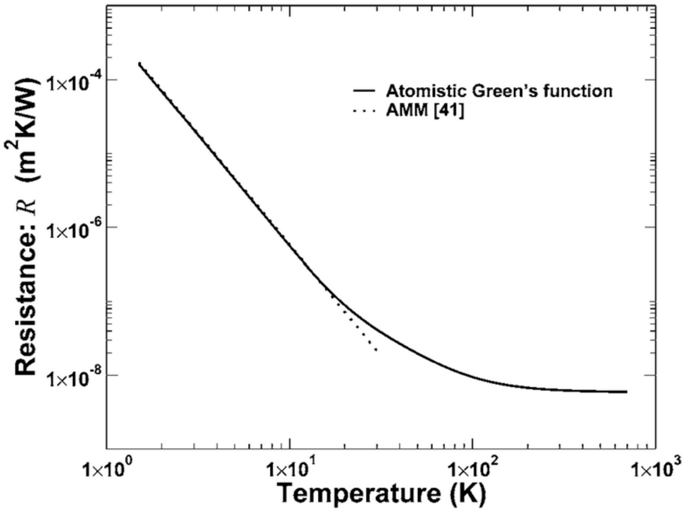

FIG. 11: Comparison of thermal boundary resistance across a Si/Ge interface calculated by atomistic Green's function method to that by the acoustic mismatch model. (Reprinted with permission from ASME, Copyright 2007).[27]

property of phonon vibrational modes. Recall that the phonon transmission function of Si/Ge interface is weighted by the phonon escape probability at angular frequency ω and wavevector $\vec{k_{||}}$ in Eq. (98). In order to show the derivation clearly, we recall the definitions of Γ_1 and Γ_2

$$\Gamma_1 = \tau_{\text{LC,LD}} a_{\text{LC}} \tau^{\dagger}_{\text{LC,LD}} \quad \Gamma_2 = \tau_{\text{RC,RD}} a_{\text{RC}} \tau^{\dagger}_{\text{RC,RD}} \tag{100}$$

where a_{LC} and a_{RC} are submatrices corresponding to the regions LC and RC of the full uncoupled spectral function matrices a_1 and a_2, respectively. $a_{\text{L(R)C}}$ is a matrix proportional to phonon density of states and is a linear combination of phonon vibrational polarizations. Hence, the crucial step in decomposing the transmission function is to break up the matrix $a_{\text{L(R)C}}$ into a series of polarization-specific components. $a_{\text{L(R)C}}$ is Hermitian ($a_{\text{L(R)C}} = i[g_{\text{L(R)C}} - g^{\dagger}_{\text{L(R)C}}] = -i[g^{\dagger}_{\text{L(R)C}} - g_{\text{L(R)C}}] = a^{\dagger}_{\text{L(R)C}}$) and can therefore be written in terms of its eigenvalue and eigenvector sets as follows:

$$a_{\text{L(R)C}} = \sum_i \lambda_{\text{L(R)C},i} \phi_{\text{L(R)C},i} \phi^{\dagger}_{\text{L(R)C},i} \tag{101}$$

where $\phi_{\text{L(R)C},i}$ are eigenvectors of matrix $a_{L(R)C}$ and $\lambda_{L(R)C,i}$ are the corresponding eigenvalues and can be interpreted as amplitudes. We define two polarization-based phonon escape rates

$$\gamma_{1,i}(\omega, \vec{k_{||}}) = \tau_{\text{LC,LD}} \lambda_{\text{LC},i} \phi_{\text{LC},i} \phi^{\dagger}_{\text{LC},i} \tau^{\dagger}_{\text{LC,LD}} \tag{102}$$

$$\gamma_{2,i}(\omega, \vec{k_{||}}) = \tau_{\text{RC,RD}} \lambda_{\text{RC},i} \phi_{\text{RC},i} \phi^{\dagger}_{\text{RC},i} \tau^{\dagger}_{\text{RC,RD}} \tag{103}$$

where i is an index number for the eigenvectors. By substituting Γ_1 and Γ_2 with $\gamma_{1,i}$ and $\gamma_{2,j}$, we obtain the transmissivity for phonon transmission from polarization i in the left contact to polarization j in the right contact as

$$\mathcal{T}_{i,j}(\omega, \vec{k_{||}}) = \mathrm{Tr}[\gamma_{1,i} G_d \gamma_{2,j} G_d^{\dagger}] \tag{104}$$

This result, which is similar in form to the overall transmission function [see Eq. (67)] illustrates the utility of the spectral functions (both coupled and uncoupled) from which the γ matrices originate and which enable high-fidelity spectral transmission information from the AGF method.

Figure 12 shows plots of polarization-specific transmission function for a thin film of Ge embedded between two semi-infinite Si contacts (see Ref. 47). The transmission function corresponds to $k_x = k_y = 0$. The transmission function for the transverse acoustic (TA) mode drops to zero at a frequency near 30 THz, and only the longitudinal acoustic (LA) mode has a nonzero transmission beyond this frequency. Also, the transmission function is close to unity for all branches at low phonon frequencies. This result is a direct consequence of the fact that long-wavelength phonons are essentially blind to the existence of the device and pass through it unhindered.

4.2 Anharmonic Extension of the AGF Method

Including anharmonicity is a challenge for the AGF method, but can also complete the method. A few published studies[26,48] extended the AGF method to include anharmonicity

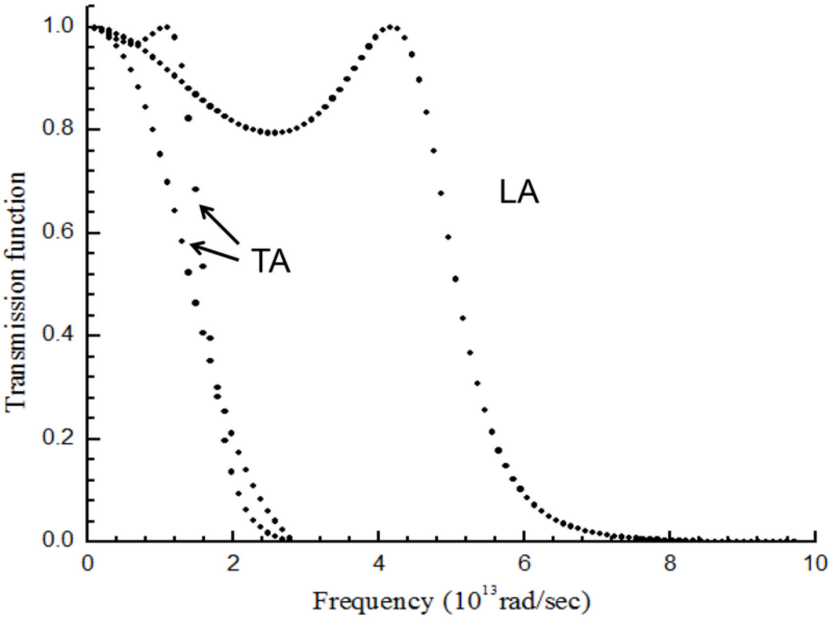

FIG. 12: Polarization resolved phonon transmission function at a Si-Ge-Si interface for $k_x = k_y = 0$. (Reprinted with permission from ASME, Copyright 2011).[47]

by using Keldysh nonequilibrium Green's function formalism.[31,37] The formalism is a very powerful tool that can simulate inelastic evolution in a system. Prior work[49] has used it to address problems such as inelastic electron tunneling. The formalism can also be extended to describe anharmonic phonon interactions.

The Hamiltonian that describes the energy of an anharmonic system is given by

$$H = \sum_{i,j} \frac{1}{2} k_{i,j} u_i u_j + \sum_i \frac{1}{2} M_i \dot{u}_i \dot{u}_i + \sum_{i,j,k} k_{i,j,k} u_i u_j u_k + \ldots \tag{105}$$

where the first two terms on the right-hand side are purely harmonic [Eq. (41)], whereas the third term is added to include the anharmonic interactions of three-phonon scattering processes: $k_{i,j,k} = (1/3!)(\partial^3 E/\partial u_i \partial u_j \partial u_k)$, where E is the total energy, u is the atomic displacement, and i, j, k are indices of atoms. Higher order contributions to the Hamiltonian are usually small compared to the third-order interaction and can be ignored. Equation (98) calculates the phonon transmission by estimating the trace of the matrix that is the product of device Green's function and broadening matrices Γ. The self-energy matrix Σ is required in the calculation of both broadening matrices and the device Green's function. In the inelastic case, the contribution of anharmonicity must be added to the self-energy term

$$\Sigma = \Sigma_1 + \Sigma_2 + \Sigma_M \tag{106}$$

where the harmonic self-energies Σ_1 and Σ_2 remain the same as before and Σ_M is the self-energy due to many-body interactions. The details involved in obtaining the many-body self-energy are discussed and demonstrated by Mingo[26] and Li et al.[48] Unlike harmonic self-energies, which can be calculated independent of the device Green's function, the computation of the many-body self-energy requires a self-consistent calculation. A flow chart of such a self-consistent calculation is shown in Fig. 13. In the first iteration, Σ_M is set to zero when the contacts and device Green's functions are computed. The computed device Green's function is used to estimate the many-body self-energy, which is then used to calculate the device Green's function again. The iterations stop when the many-body self-energy Σ_M and the device Green's function G_d achieve self-consistency.

Mingo[26] used a molecular-sized junction to demonstrate the computational process. Empirical potentials were used in obtaining the third-order interactions. The anharmonic effect grows stronger as temperature increases. Figure 14 shows the variation of $-\Delta\sigma/\sigma = -(\sigma_a - \sigma_h)/\sigma_h$ with temperature, where σ_h is the harmonic junction's conductance and σ_a is the conductance including anharmonic interactions. The results show that the reduction in thermal conductance because of inelastic scattering is $\sim$20% at 300 K. The "classical" results are calculated by reducing the reduced Planck constant ($\hbar$) 10 times in order to achieve a linear relation between $-\Delta\sigma/\sigma_h$ and temperature, by limiting the spatial extension of wave functions. The nonzero $-\Delta\sigma/\sigma_h$ at low temperatures for the "regular" calculation is explained by the uncertainty principle, which dictates that the lattice vibration has a finite amplitude even at zero temperature due to the third-order modification of the potential.

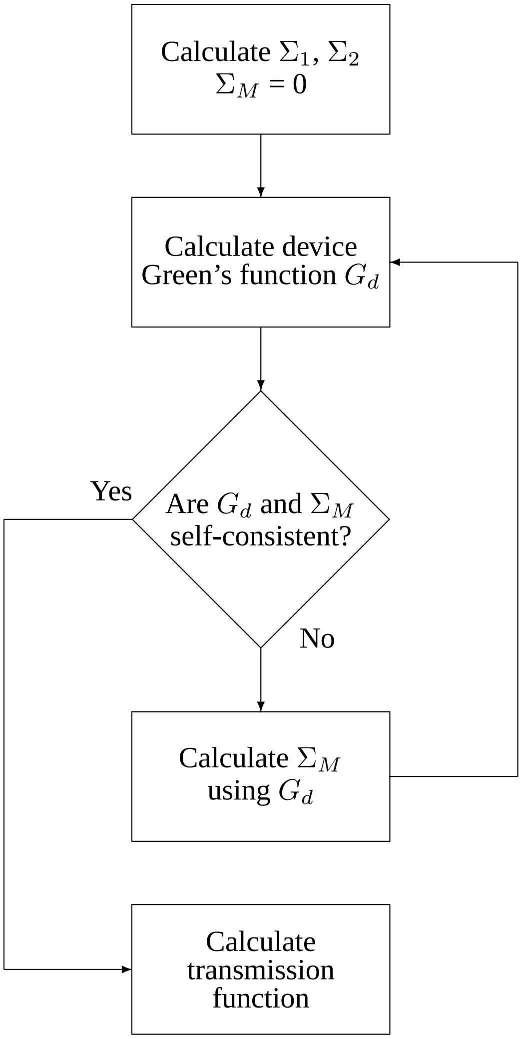

FIG. 13: Self-consistent calculation process for computing self-energy matrices and Green's functions in an anharmonic system.

4.3 Integrated Transport Solvers

As discussed in Section 2, the AGF method is founded on the harmonic matrix, which in turn requires the definition of interatomic potentials that are often not available, especially for interactions of atoms across a heterogeneous interface. For such cases, first-principles-based methods can be used to calculate the interatomic force constants (IFCs) that can be used as inputs for the AGF calculation. In the first part of this section, we demonstrate this process using a DFT-incorporated AGF solution of a TiC-GNR structure. We also discuss a method to optimize the DFT-calculated IFCs before using them in an AGF calculation.

The AGF method is only amenable for systems in which phonons show strong wave behavior. However, a complex system could include more than one computational scale

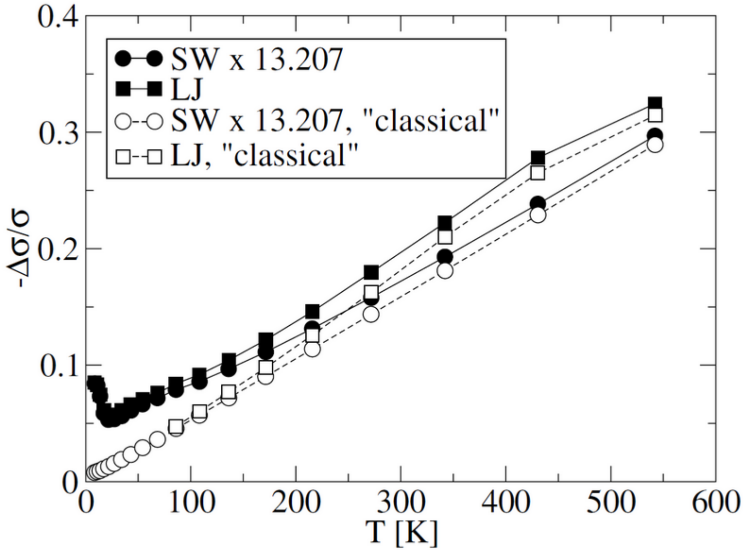

FIG. 14: Relative decrease in thermal conductance as a function of temperature due to anharmonicity. (Reprinted with permission from American Physical Society, Copyright 2006).[26]

where phonons could behave as a wave or particle, depending on the length scale of interest. The AGF method is not appropriate in solving transport problems that involve length scales many times larger than phonon wavelength. Instead, a particle-based solution is needed. The BTE is a mesoscopic transport model and has been used to solve phonon transport in systems with dimensions that are many times longer than the dominant phonon wavelengths. However, BTE-based solutions usually resort to simplified interface models, such as AMM or DMM,[50] to estimate phonon transmission/reflection at interfaces. The AGF method can provide polarization-specific transmission information that can be used as input to BTE solvers. In Section 4.3.1, we demonstrate the integration of AGF and BTE methods with a Si-Ge interface as an example.

4.3.1 Integration of DFT with AGF Simulation

A DFT-incorporated AGF solver is developed here to study phonon transport through a heterogeneous interface between bulk TiC substrates and GNRs. DFT provides IFCs for TiC and GNRs. The goal is to demonstrate that the two methods can be integrated to solve complicated interface transport problems. The IFCs of TiC are calculated using the density functional perturbation theory[51,52] (DFPT) software Quantum ESPRESSO, given the previous success by Iseav et al.[53] The IFCs for GNRs are calculated by SIESTA[44] using the approach of Gillen et al.[54] Attempts to resolve the TiC-GNR atomic positions and related IFCs were made by DFT (SIESTA), but convergence of the electronic energy ground states did not occur. There is no prior work to our knowledge that has reported success in obtaining IFCs for TiC-GNR interfaces from first-principles DFT. However, previous DFT work has reported electron density distributions of CNTs adsorbed on Si substrates,[55,56] though no IFCs, which involve significantly more computational effort, were calculated. Although DFT cannot provide atomic positions or the IFCs of TiC-GNR interface atoms, future AGF work should attempt using DFT-predicted interface atomic structure and force constants to solve phonon transport in a contact-device-contact—like system. Such software for electron transport has already been built [e.g., TranSIESTA (Ref. 57)]. Similar tools are crucial for the thermal engineer to solve generic nanoscale phonon transport problems.

The integration of AGF and DFT is very difficult in practice, especially when no atomic positions or IFCs at the interface are provided from DFT. Simplified models can be used to overcome the challenges. DFT calculates force constants between an atom and its nth nearest neighbor in which n can be very large. It is computationally inefficient to employ all such interactions in Green's function calculations, because many long-range interactions are weak. Therefore, a cutoff distance is typically imposed such that it is long enough to replicate known vibrational properties of a material. Upon truncation, force constants are adjusted to ensure harmonicity and to satisfy the acoustic sum rule.[39] The phonon disperson curves of TiC and GNR are calculated using the truncated IFCs. The results show that only small errors are introduced by the truncation.[41]

To further simplify the calculation, the GNR unit cell at each end of the device is strained in the ribbon's width direction so that the C-C bond length matches half of the face diagonal distance of the TiC unit cell. The rest of the unit cells in the GNR and all unit cells in the contacts remain unstrained. A schematic view of a TiC-GNR-TiC structure is shown in Fig. 15(a), where the cyan atoms are C, green atoms are Ti, and red atoms are H. The structure in Fig. 15(a) is represented by TiC-8GNR-TiC where 8 is the number of carbon dimers in a GNR unit cell. In this case, TiC substrates are the contacts and the GNR is denoted as the device. Because the armchair edges of GNRs are connected to the contacts, the hydrogen-passivated edges of the GNR device are in the zigzag configuration. The atomic positions in the x-z plane containing the GNR are shown in Fig. 15(b).

The shortest distance between surface Ti and C atoms in the GNR is set to be 2.13 Å, which is the Ti-C bond length in TiC [see Fig. 15(b)]. The force constants are cut off beyond 4.26 Å between atoms in the contacts and the device. However, longer range Ti-C interactions exist at the interfaces, and for these, a correction is introduced by reducing these force constants by a factor of d^2/d_o^2, where d_o is the actual distance between Ti and C atoms at the interface and d is the largest Ti-C distance (less than d_o) in a pure TiC crystal. This type of quadratic correction can be found in the two-body term of Harrison potential.[58] Also, the changes in IFCs because of the strain in GNR unit cells at interfaces are handled according to the method introduced by Chen and Wang.[59]

After obtaining the force constants, the harmonic matrices of the system are computed and used as inputs for the Green's function calculation as described by Zhang et al.[35] A TiC-GNR setup studied and is intended to approximate an interface between TiC and a long unzipped CNT. The conductances of the TiC-GNR cases are shown in Fig. 16(a), and the conductances normalized by GNR width are shown in Fig. 16(b). We use the converged result in Fig. 16(b) to estimate the interface thermal conductance of TiC-CNT interfaces. The results show that the normalized conductance tends toward a value of 0.25 W/mK as the GNR width is increased. At room temperature, Xu and Fisher[2] estimated the

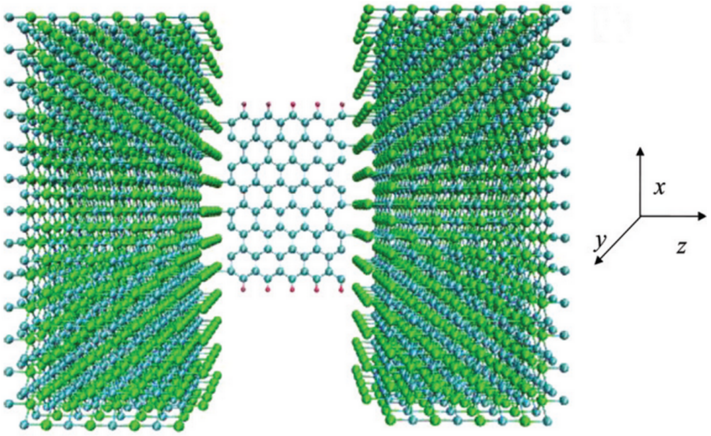

(a) 3D view

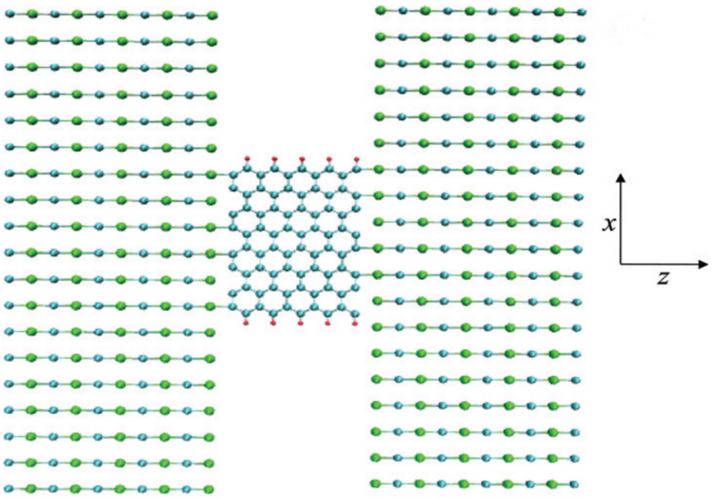

(b) Atoms in GNR plane

FIG. 15: Schematic view of a $m = 5$ TiC-8GNR-TiC structure. (Reprinted with permission from American Institute of Physics Publishing LLC, Copyright 2011).[41]

average diameter of multiwalled CNTs (MWCNTs) in their CNT arrays to be 30 nm (with a corresponding circumference near 100 nm). Therefore, interfacial thermal conductance between the outer wall of a MWCNT and TiC is approximately 2.5×10^{-8} W/K. The density of vertical CNT arrays synthesized in the experiment was $\approx 10^8$ CNTs/mm^2.[2] On the basis of the AGF results, the estimated thermal resistance for such a MWCNT array is 0.4 mm^{2}K/W, assuming that the outer walls dominate thermal transport.[60] Importantly, this value agrees in an order-of-magnitude sense with the experimental results of Cola et al.,[61] who used a photoacoustic technique to determine the local CNT-substrate interface thermal resistance.

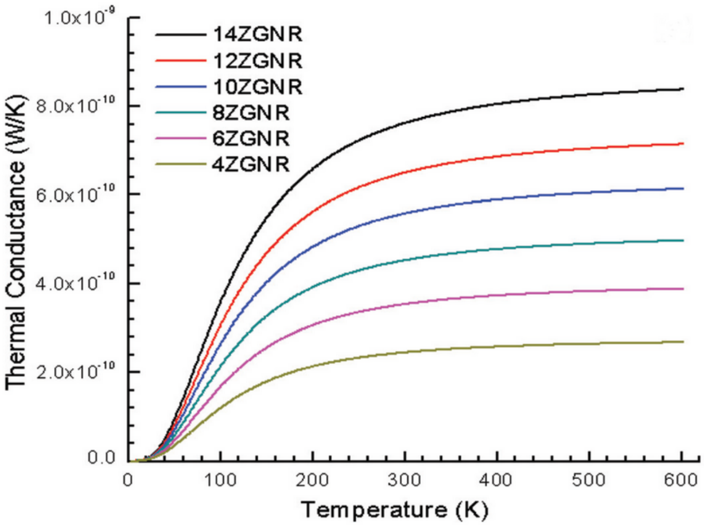

(a) Thermal conductance of single contact TiC-GNR interfaces

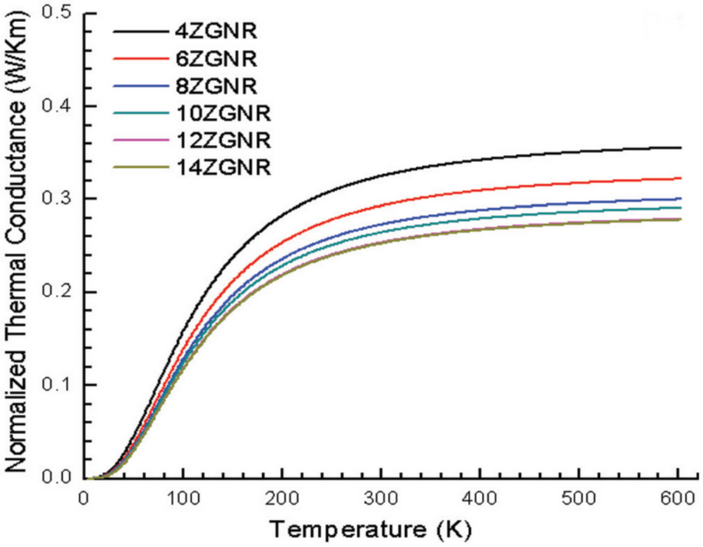

(b) Thermal conductance normalized by ribbon width

FIG. 16: Thermal conductance of TiC-GNR-TiC interfaces. (Reprinted with permission from American Institute of Physics Publishing LLC, Copyright 2011).[41]

4.3.1.1 Optimization of Raw DFT IFCs

DFT calculations do not impose a cutoff distance for interactions among atoms. However when using DFT-derived force constants in AGF simulations, a suitable cutoff distance is often imposed. In the truncation process, small interactions are ignored and this may lead to unphysical results at low frequency.[39] For instance, the rotation mode of a nanowire or nanotube structure will likely vanish because the truncation destroys the symmetry invariance of the harmonic matrix. Therefore, the raw IFCs obtained from DFT calculations must be optimized to provide physically correct results in LD calculations. Mingo et al.[39] introduced a procedure to symmetrize the force constants matrix by adding a correction matrix. The correction matrix is very small compared to the original force constants matrix. Following the notation of Ref. 39, the new force constants matrix ($\tilde{K}_{ij}$) is given by

$$\tilde{K}_{ij} = K_{ij} + D_{ij} \tag{107}$$

where K_{ij} is the IFCs matrix obtained from raw DFT results and D_{ij} is the correction matrix. An error function is defined to measure the change that is introduced by the correction matrix

$$f = \sum_{i,j} \frac{D_{ij}^2}{K_{ij}^2} \tag{108}$$

The new force constants matrix must be invariant with respect to rigid translations and rotations of the system. The mathematical conditions for such invariance are given by

$$\sum_{j} (K_{ij} + D_{ij}) R_j^n = 0 \tag{109}$$

where n is the label for translational or rotational degrees of freedom and R_j^n are the displacement vectors. The physical meaning of Eq. (109) has been explained by Mahan and Jeon.[62] The problem of estimating the elements of correction matrix D is a constrained optimiztion problem with the objective function to be minimized given by the error function in Eq. (108) and the constraints being given by Eq. (109). Mingo et al.[39] proposed the use of Lagrange multipliers, a standard technique in constrained optimization, to estimate the elements of the correction matrix. They also pointed out alternative techniques, such as geometrical distance minimization,[63] that can be used to optimize the raw DFT results to satisfy translational and rotational invariance.

4.3.2 AGF-BTE

The transmission function calculated by the AGF method can be used as an interface condition in a BTE simulation. Energy conservation is enforced at the interface where the energy carried by the phonon is either transmitted through or reflected. Here, a finite volume scheme is used to solve the BTE in a domain with a Si/Ge interface.[64] The domain is divided into control volumes, and an energy balance is written for each control volume and its frequency band and polarization. The energy flow is treated as a heat source/sink term in the cells next to the interface. A schematic view of interface treatment and energy balance is shown in Fig. 17. The heat flux [Eq. (110)] of a frequency band i obtained from AGF results is treated as a source/sink term in BTE, which only affects the cells next to the interface

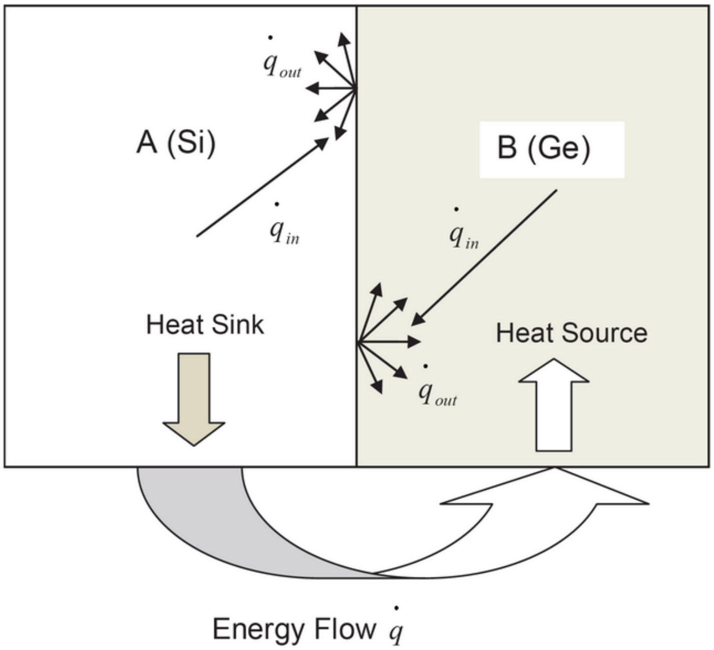

FIG. 17: Energy boundary condition at Si/Ge interface. (Reprinted with permission from Cambridge University Press, Copyright 2009).[64]

$$\dot{q}_i = \int\limits_{\Delta\omega_i} \frac{\hbar\omega}{2\pi}\mathcal{T}(\omega)\frac{\Delta f_{\text{BE}}^{o}}{\Delta T}d\omega \tag{110}$$

where the transmission function $\mathcal{T}(\omega)$ is obtained from the AGF calculation. $\Delta T = T_1 - T_2$ is obtained from the BTE simulation, $\Delta f_{\text{BE}}^{o} = f_{\text{BE}}^{o}(\omega, T_1) - f_{\text{BE}}^{o}(\omega, T_2)$ is the difference in Bose-Einstein distribution between control volumes on either side of the interface. The heat flux is distributed to each direction and polarization in proportion to the solid angles and the phonon specific heat fractions

$$\dot{q}_{i,p,j} = \frac{\Delta\Omega_j}{4\pi}\frac{C_p(\omega_i)}{\sum\limits_{p} C_p(\omega_i)}\int\limits_{\Delta\omega_i} \frac{\hbar\omega}{2\pi}\mathcal{T}(\omega)\frac{\Delta f_{\text{BE}}^{o}}{\Delta T}d\omega \tag{111}$$

where $\Delta\Omega_j$ is the solid angle and i, p are the indices for frequency band and polarization, respectively. Note that there are many ways that can be used to distribute the heat flux to different polarizations and solid angles other than Eq. (111). It can be changed to optimize the convergence speed of calculation.

The effective thermal conductivity of a Si/Ge interface was investigated as a function of domain size to demonstrate the feasibility of integrating the AGF and BTE methods. The results in Fig. 18 revealed that thermal conductivity increases with L; such a result is expected because the heat flux is constant with L in the ballistic limit, leading to a thermal conductivity that scales linearly with L.

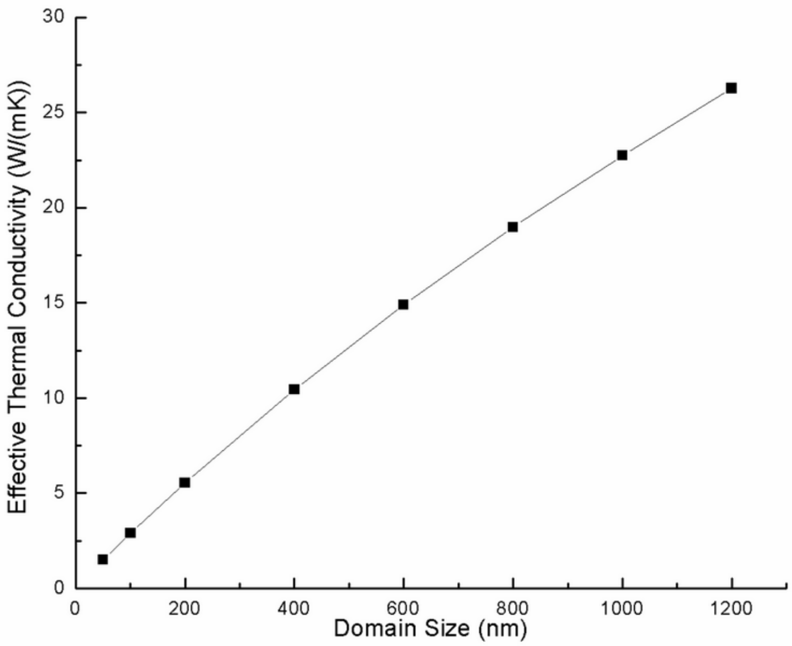

FIG. 18: Effective thermal conductivity of a Si/Ge interface as a function of domain size. (Reprinted with permission from Cambridge University Press, Copyright 2009).[64]

4.4 Comparison to Experimental Measurements

Advanced experimental techniques such as time-domain thermoreflectance method,[9] the 3ω method,[8] and photoacoustic method[61] allow measurements of thermal conductivity and interfacial thermal conductance in nanoscale structures. In the last decade, many studies have been reported for the thermal properties measurement of superlattice thin films,[8,65–72] nanowires,[67,73–76] and other nanostructured materials.[2,61,77–84] In this section, we discuss some of these experimental measurements on superlattice thin films[65,66,68,72] and carbon nanostructures[2,61,77–84] and compare them to the numerical results computed from the AGF simulations in order to illustrate the advantages and limitations of the AGF method.

4.4.1 Thin-Film Superlattice

A thin-film superlattice consists of alternating layers of two different materials stacked on each other. Thermoelectric materials made of thin-film superlattices have been widely studied because they are very promising for energy conversion and thermal management applications. Superlattices provide avenue to investigate fundamentals of phonon transport such as coherent transport and transition from the ballistic-to-diffusive transport due to the periodic structures of thin films. Recently, a study by Luckyanova et al.[72] has demonstrated coherent heat conduction in GaAs/AlAs thin-film superlattices by measuring the thermal conductivity of finite-thickness superlattices with varying numbers of periods (Fig. 19).

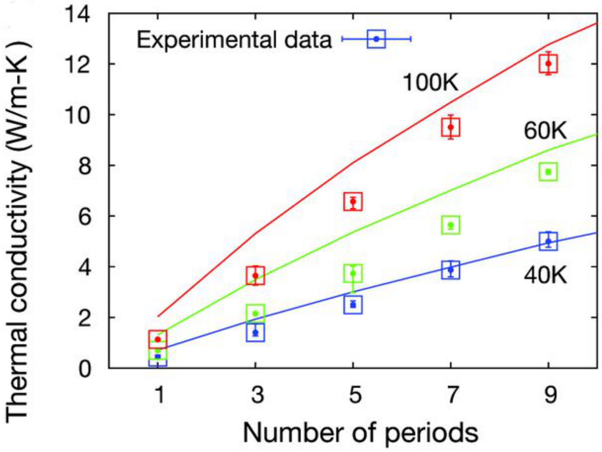

FIG. 19: Thermal conductivity of GaAs/AlAs superlattice as a function of number of periods at 40, 60, and 100 K. Solid lines correspond to the AGF simulations for rough interfaces and dots with error bars correspond to the experimental measurements. (Reprinted with permission from American Association for the Advancement of Science, Copyright 2012).[72]

Superlattices with thin layers and periodic interfaces can be treated as a new homogenous material, whose phonon dispersions are modified due to the interference of coherent phonon waves. Some phonons can travel ballistically through the superlattice and are scattered only at the boundary rather than at interfaces as their wavelength is much larger than the length scales of the interface roughness. The phonon mean free path of these phonons increases with the number of periods or the total length of the superlattice, which can lead to an increase of thermal conductivity with the number of periods. Luckyanova et al.[72] observed a linear increase in the superlattice thermal conductivity with the number of periods or total thickness of the superlattice (Fig. 19) in the temperature range of 30 – 150 K, which confirmed the coherent heat conduction in these structures. They also performed AGF simulations to demonstrate the dominant role of coherent phonon transport in superlattices. They fabricated samples of superlattices with 1, 3, 5, 7, and 9 periods sandwiched between semi-infinite Al and GaAs leads and also used the similar structures in the AGF simulations. The interface roughness in the AGF simulations was created by randomly shuffling Ga and Al atoms within a layer of interface, but the lattice mismatch was not fully considered. The temperature dependence of the thermal conductivity in the coherent transport regime was observed to be consistent with the experimental results. However, to obtain reasonable quantitative agreement with the experiments (as shown in Fig. 19), the interfacial thermal resistance between Al contact and superlattice was artificially increased by an order of magnitude by modifying the force constants and masses of atoms. Such treatment in the AGF simulations is reasonable because roughness of interfaces at superlattice boundaries in samples is difficult to predict and image. Irrespective of such treatment of the boundaries, AGF provides crucial insights into coherent phonon transport and transmission across multiple interfaces in the superlattice. The analysis by Luckyanova et al.[73] using

AGF simulations showed small variations in the transmission of low-frequency phonons with increasing periods of superlattice, but the transmission of high-frequency phonons decreased as the number of periods increased. This analysis deciphered an important phonon transport mechanism in thin-film superlattices (i.e., that interface roughness destroyed the coherence of high-frequency phonons but not of the low-frequency phonons).

Li and Yang[42] studied phonon transmission across a lattice-mismatched interface by integrating the molecular dynamics and AGF based methods. They compared the computed thermal conductance at Si/Ge interface against the experimental measurements,[65,66] as shown in Fig. 20. They observed that the thermal conductance at Si/Ge interfaces annealed at 300, 1000, and 1500 K fall between the experimentally measured conductances of superlattices with periods of 14.0 and 27.5 nm. They observed a better agreement between simulation and experimental measurements for the superlattice of 27.5 nm period. This is consistent because their AGF simulations used interfaces formed by two bulk materials that can be expected to be closer to the superlattice with larger period thickness. The deviation of AGF predictions from the experimental values, as depicted in Fig. 20, can be attributed to the use of an empirical force field model, neglecting anharmonic scattering in Green's function calculation and different interface conditions in the experimental

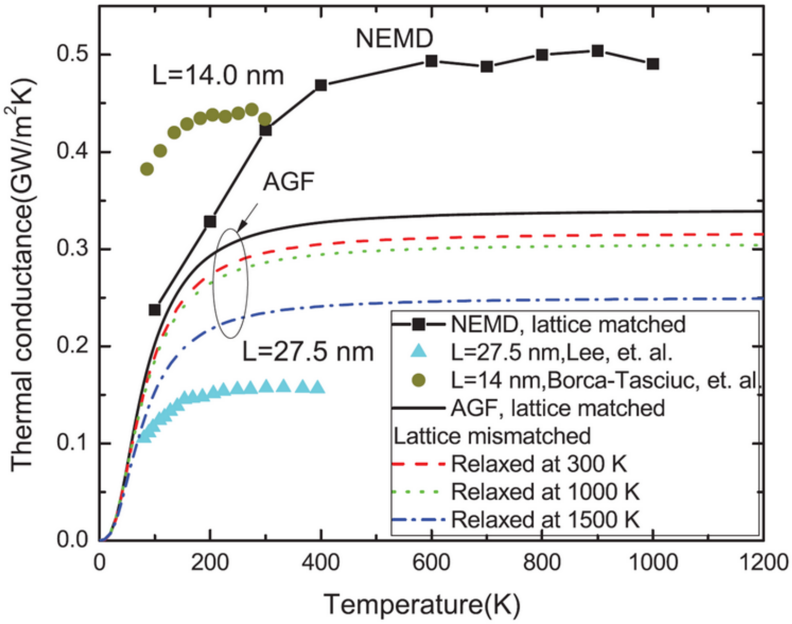

FIG. 20: Comparison of thermal conductance at Si/Ge interface estimated from the AGF simulations, non-equilibrium molecular dynamics (NEMD) simulations, and experiments. The period thickness (L) of Si/Ge superlattice is 14.0 nm and 27.5 nm in the experimental measurements by Lee et al.[65] and Borca-Tasciuc et al.,[66] respectively. Lattice-mismatched structures of Si/Ge interface for AGF calculations were prepared by annealing the structure at 300 K, 1000 K, and 1500 K. (Reprinted with permission from American Physical Society, Copyright 2012).[42]

samples. In a separate study, Zhang et al.[27] also compared experimental results from Ref. 66 to their AGF calculations of Si/Ge interfacial thermal conductance in a superlattice with a 3 nm period at 200 K. The thermal conductance calculated by the AGF method for a superlattice of total thickness <50 nm is approximately one order of magnitude larger than the experimentally measured conductance. Interface roughness, lattice mismatch, and coherent phonon transport through the thin periods are the main reasons for this large deviation compared to the experiments.

4.4.2 *Graphene and Carbon Nanotube Interfaces*

The AGF method has been also used to elucidate thermal transport at the interface of carbon nanostructures such as graphene and carbon nanotube. Graphene, a 2-D monolayer of sp^2 bonded carbon atoms, has high intrinsic thermal conductivity, but the thermal conductance at the graphene interfaces with other materials vary in a large range.[77,78,80–82,85,86] Low thermal conductance at graphene interfaces may lead to thermal management issues in nano-electronic devices. Several studies[77,78,80–82,86] have been performed to measure the thermal conductance at graphene (graphite) interfaces with different metals. These measurements show (Fig. 21) that the thermal conductance at graphene (graphite) interfaces with Ti and Cr is much higher than with Au. This indicates two different types of interface interactions, depending on the chemical bonding at the graphene interface with metals. Graphene can form two different types of interfaces with metals: a physisorption

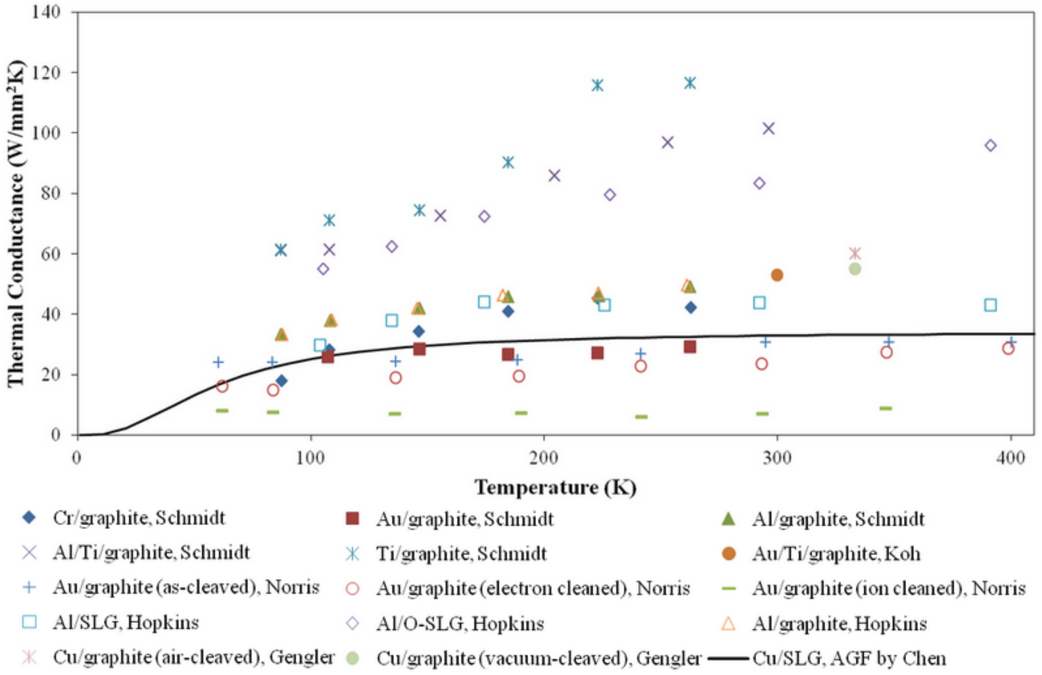

FIG. 21: Thermal conductance at metal-graphite or metal-graphene interfaces. Experimental data is taken from Refs. 78, 80–82, and 86.

interface by charge transfer or a chemisorption interface by orbital hybridization. The interactions at physisorption interfaces is weak and dominated by the van der Waals (vdW) forces, whereas strong metal carbide bonding can be formed at the chemisorption interfaces. The nature of surface chemical bonding can dramatically change the interface thermal conductance as reported by Norris et al.[81] (see Fig. 21). Interface preparation methods can also significantly change the contact conductance. The highest thermal conductance at the Au-graphene (graphite) interface was measured for as-cleaved graphite, followed by electron cleaned and ion-cleaned interface. Besides the chemical bonding and interface roughness, phonon spectrum mismatches can significantly reduce interfacial thermal conductance. Metals like Cu and Ti have negligible phonon DOS above 10 THz, but the DOS of graphene is up to 50 THz. This mismatch in DOS between graphene and metals may restrict the phonon transmission to low-frequency phonon modes. The AGF method can be employed to investigate the transmission of different phonon modes across the interface and to estimate the contribution of different phonon modes to interface thermal conductance. The method is powerful for such analysis as accurate force constants computed from the first-principles calculations can be easily incorporated, and the effect of different interface structures can be studied. Chen et al.[87] investigated the phonon transport in single-layer graphene sandwiched between two surfaces of Cu (111) substrates, and determined the thermal conductance using the AGF method. The equilibrium structure and force constants for all the interactions were obtained from DFT calculations. The thermal conductance for a single graphene/Cu interface was calculated to be 33 MW/m^{2}K at 300 K when the graphene lattice constant is matched with Cu. In experimental measurements by Gengler et al.,[86] the thermal conductance is 60 MW/m^{2}K and 55 MW/m^{2}K for the air-cleaved and vacuum-cleaved samples, respectively. The temperature in their experiments varied from 328 to 343 K ($\sim$330 K is used in Fig. 21). Considering the complicated interface structure formed using different cleaning methods and metal deposition techniques, the predicted interface conductance value is in reasonable agreement (Fig. 21) with the measurements by Gengler et al.[86]

Similar to graphene, CNTs have high intrinsic thermal conductivity along the tube axis and have been extensively studied for potential use in energy conversion, energy storage, and thermal management applications. Despite a high thermal conductivity, the high thermal resistance between nanotube tips and substrates limits its performance as thermal interface material for thermal management. Several different methods have been employed to measure the thermal resistance of carbon nanotube arrays grown on different substrates. Xu and Fisher[2] measured the resistance of CNT arrays grown on Si substrate by plasma-enhanced chemical vapor deposition using Ti/Al/Fe metal layer as catalyst. They reported a dry contact resistance of 20 mm^{2}K/W, which included the resistances at CNT-substrate interfaces and the CNT array's bulk resistance. Hu et al.[79] used a three-omega (3ω) method to measure the thermal resistance of CNT array synthesized by the same method and reported a room temperature thermal resistance of 14 mm^{2}K/W. Tong et al.[83] used a transient thermoreflectance method and measured a thermal resistance of 1 mm^{2}K/W for CNT arrays grown on Si substrate and welded to a glass plate using a layer of indium. For CNT arrays grown on Si substrate using Ti as catalyst, Zhang et al.[84] reported a thermal resistance of 7 $\mathrm{mm}^2\mathrm{K/W}$. Disagreements between the experimental measurements and AGF predictions[41] can be primarily attributed to the simplified interface structures in the AGF simulations. The contact structure for CNT arrays grown on a Si substrate can be complicated (i.e., many CNTs may not make contact with the substrate and many of them may make little or no physical contact leading to a large variation in the contact structure and interfacial resistance from one CNT contact to another). The metal layer of Ti/Al/Fe catalyst in experimental samples was amorphous or polycrystalline rather than the single crystalline as in Huang's study.[41] The nanotubes in Xu and Fisher's study[2] were multi-walled, so effective contact area of the CNTs has been significantly reduced if the heat is conducted primarily through the outer wall. The defects in nanotubes may have further increased their overall thermal resistance. All these factors may be the reasons for the disagreements between the AGF predictions and experimental measurements.

5. CONCLUSIONS AND OUTLOOK

This chapter has elucidated the basic methodology of the harmonic form of the atomistic Green's function with particular emphasis on concepts that appeal to the intuition of engineers (such as the continuum form as an introduction) and elucidation of critical details of the method, mainly involving, where possible, an explanation of the physical meaning of the various matrices (and submatrices) that are essential to the method. It has further highlighted extensions of the method that, we hope, will promote its wider adoption. These extensions include the effects of interatomic bond anharmonicity, multiscale model integration through the DFT-derived inter-atomic bonding and AGF-derived transmission functions, treatment of interfaces with dimensional discontinuities, and extraction of polarization-specific spectral information.

The penultimate section has highlighted the correlation between AGF models and experimental results. Although promising agreement exists, much work remains in order for this simulation approach (and others) to graduate to a truly predictive role in thermal engineering. The main obstacles remain uncertainty of local interatomic bonding at heterogeneous interfaces and unknown local geometries (e.g., lattice orientation, contact area) in practical interfaces that are inherently rough and/or contain many nanoscale objects, such as carbon nanotubes. Given these limitations, future attention should focus on atomic-scale imaging (e.g., transmission electron microscopy) and chemical analysis (e.g., electron spectroscopies), as well as robust process models that can predict with quantitative, statistical confidence such heterogeneous interface geometries, without resorting to complex, expensive, and time-consuming experiments.[88] For all such developments, closer collaboration among experimentalists and theorists, and among scientists and engineers, will be essential.

ACKNOWLEDGMENTS

This material is based on work supported by the US Office of Naval Research under Award No. N00014-12-1-1006. The authors also thank Prof. Supriyo Datta for illuminating discussions on the NEGF method.

REFERENCES

1. D. G. Cahill, W. K. Ford, K. E. Goodson, G. D. Mahan, A. Majumdar, H. J. Maris, R. Merlin, and S. R. Phillpot, Nanoscale thermal transport, *J. Appl. Phys.*, 93:793–818, 2003.
2. J. Xu and T. S. Fisher, Enhancement of thermal interface materials with carbon nanotube arrays, *Int. J. Heat Mass Transfer*, 49:1658–1666, 2006.
3. A. M. Pettes, M. S. Hodes, and K. E. Goodson, Optimized thermoelectric refrigeration in the presence of thermal boundary resistance, *IEEE Trans. Adv. Pack.*, 32:423–430, 2009.
4. I. Chowdhury, R. Prasher, K. Lofgreen, G. Chrysler, S. Narasimhan, R. Mahajan, D. Koester, R. Alley, and R. Venkatasubramanian, On-chip cooling by superlattice-based thin-film thermoelectrics, *Nat. Nanotechnol.*, 4:235–238, 2009.
5. A. I. Hochbaum, R. Chen, R. D. Delgado, W. Liang, E. C. Garnett, M. Najarian, A. Majumdar, and P. Yang, Enhanced thermoelectric performance of rough silicon nanowires, *Nature*, 451:163–167, 2008.
6. K. Schwab, E. Henriksen, J. Worlock, and M. Roukes, Measurement of the quantum of thermal conductance, *Nature*, 404:974–977, 2000.
7. L. G. Rego and G. Kirczenow, Quantized thermal conductance of dielectric quantum wires, *Phys. Rev. Lett.*, 81:232–235, 1998.
8. D. G. Cahill, M. Katiyar, and J. Abelson, Thermal conductivity of α-Si:H thin films, *Phys. Rev. B*, 50:6077–6081, 1994.
9. D. G. Cahill, Analysis of heat flow in layered structures for time-domain thermoreflectance, *Rev. Sci. Inst.*, 75:5119–5122, 2004.
10. W. A. Little, The transport of heat between dissimilar solids at low temperatures, *Can. J. Phys.*, 37:334–349, 1959.
11. E. T. Swartz and R. Pohl, Thermal boundary resistance, *Rev. Mod. Phys.*, 61:605–668, 1989.
12. E. T. Swartz and R. O. Pohl, Thermal resistance at interfaces, *Appl. Phys. Lett.*, 51:2200–2202, 1987.
13. R. S. Prasher and P. E. Phelan, A scattering-mediated acoustic mismatch model for the prediction of thermal boundary resistance, *J. Heat Transfer*, 123:105–112, 2001.
14. R. Prasher, Acoustic mismatch model for thermal contact resistance of van der Waals contacts, *Appl. Phys. Lett.*, 94:041905, 2009.
15. J. C. Duda, P. E. Hopkins, J. L. Smoyer, M. L. Bauer, T. S. English, C. B. Saltonstall, and P. M. Norris, On the assumption of detailed balance in prediction of diffusive transmission probability during interfacial transport, *Nanoscale Microscale Thermophys. Eng.*, 14:21–33, 2010.
16. P. Reddy, K. Castelino, and A. Majumdar, Diffuse mismatch model of thermal boundary conductance using exact phonon dispersion, *Appl. Phys. Lett.*, 87:211908, 2005.
17. M. D. Losego, M. E. Grady, N. R. Sottos, D. G. Cahill, and P. V. Braun, Effects of chemical bonding on heat transport across interfaces, *Nat. Mater.*, 11:502–506, 2012.
18. S. L. Hodson, T. Bhuvana, B. A. Cola, X. Xu, G. Kulkarni, and T. S. Fisher, Palladium thiolate bonding of carbon nanotube thermal interfaces, *ASME J. Electron. Packag.*, 133:020907, 2011.
19. P. Schelling, S. Phillpot, and P. Keblinski, Phonon wave-packet dynamics at semiconductor interfaces by molecular dynamics simulations, *Appl. Phys. Lett.*, 80:2484–2486, 2002.

20. S. G. Volz and G. Chen, Molecular-dynamics simulation of thermal conductivity of silicon crystals, *Phys. Rev. B*, 61:2651–2656, 2000.
21. L. Sun and J. Y. Murthy, Domain size effects in molecular dynamics simulation of phonon transport in silicon, *Appl. Phys. Lett.*, 89:171919, 2006.
22. M. Lumpkin, W. Saslow, and W. Visscher, One-dimensional Kapitza conductance: Comparison of the phonon mismatch theory with computer experiments, *Phys. Rev. B*, 17:4295–4302, 1978.
23. D. Young and H. Maris, Lattice-dynamical calculation of the Kapitza resistance between fcc lattices, *Phys. Rev. B*, 40:3685–3693, 1989.
24. H. Zhao and J. Freund, Lattice dynamical calculation of phonon scattering at ideal Si-Ge interfaces, *J. Appl. Phys.*, 97:024903, 2005.
25. N. Mingo and L. Yang, Phonon transport in nanowires coated with an amorphous material: An atomistic Green's function approach, *Phys. Rev. B*, 68:245406, 2003.
26. N. Mingo, Anharmonic phonon flow through molecular-sized junctions, *Phys. Rev. B*, 74:125402, 2006.
27. W. Zhang, T. Fisher, and N. Mingo, Simulation of interfacial phonon transport in Si-Ge heterostructures using an atomistic Green's function method, *ASME J. Heat Transfer*, 129:483–491, 2007.
28. Y. Chalopin, S. Volz, and N. Mingo, Upper bound to the thermal conductivity of carbon nanotube pellets, *J. Appl. Phys.*, 105:084301, 2009.
29. N. Mingo, Green's function methods for phonon transport through nano-contacts, *Thermal Nanosys. Nanomater.*, 118:63–94, 2009.
30. P. C. Martin and J. Schwinger, Theory of many-particle systems. I, *Phys. Rev.*, 115:1342–1373, 1959.
31. L. V. Keldysh, Diagram technique for non-equilibrium processes, *Sov. Phys. JETP*, 20:1018, 1965.
32. S. Datta, *Quantum Transport: Atom to Transistor*, Cambridge University Press, New York, 2005.
33. S. Datta, Electrical resistance: An atomistic view, *Nanotechnology*, 15:S433–S451, 2004.
34. S. Datta, Nanoscale device modeling: The Green's function method, *Superlattices Microstruct.*, 28:253–278, 2000.
35. W. Zhang, T. Fisher, and N. Mingo, The atomistic Green's function method: An efficient simulation approach for nanoscale phonon transport, *Numer. Heat Transfer, Part B*, 51:333–349, 2007.
36. W. Zhang, N. Mingo, and T. Fisher, Simulation of phonon transport across a non-polar nanowire junction using an atomistic Green's function method, *Phys. Rev. B*, 76:195429, 2007.
37. S. Datta, *Electronic Transport in Mesoscopic Systems*, Cambridge University Press, New York, 1995.
38. F. Guinea, C. Tejedor, F. Flores, and E. Louis, Effective two-dimensional Hamiltonian at surfaces, *Phys. Rev. B*, 28:4397–4402, 1983.
39. N. Mingo, D. Stewart, D. Broido, and D. Srivastava, Phonon transmission through defects in carbon nanotubes from first principles, *Phys. Rev. B*, 77:033418, 2008.
40. J. Y. Murthy and S. R. Mathur, Computational heat transfer in complex systems: A review of needs and opportunities, *ASME J. Heat Transfer*, 134:031016, 2012.

41. Z. Huang, T. Fisher, and J. Murthy, An atomistic study of thermal conductance across a metal-graphene nanoribbon interface, *J. Appl. Phys.*, 109:074305, 2011.

42. X. Li and R. Yang, Effect of lattice mismatch on phonon transmission and interface thermal conductance across dissimilar material interfaces, *Phys. Rev. B*, 86:054305, 2012.

43. X. Gonze, Adiabatic density functional perturbation theory, *Phys. Rev. A*, 52:1096–1114, 1995.

44. J. M. Soler, E. Artacho, J. D. Gale, A. Garcia, J. Junquera, P. Ordejon, and D. Sanchez-Portal, The SIESTA method for ab initio order-n materials simulation, *J. Phys. Condens. Matter*, 14:2745–2779, 2002.

45. Z. Huang, T. S. Fisher, and J. Y. Murthy, Simulation of phonon transmission through graphene and graphene nanoribbons with a Green's function method, *J. Appl. Phys.*, 108:094319, 2010.

46. Z. Huang, T. S. Fisher, and J. Y. Murthy, Simulation of thermal conductance across dimensionally mismatched graphene interfaces, *J. Appl. Phys.*, 108:114310, 2010.

47. Z. Huang, J. Y. Murthy, and T. S. Fisher, Modeling of polarization specific phonon transmission through interfaces, *ASME J. Heat Transfer*, 133:114502, 2011.

48. J. Li, T. A. Yeung, C. Kam, Y. Peng, Q. hu Chen, X. Zhao, and C. Q. Sun, Anharmonic phonon transport in atomic wire coupled by thermal contacts with surface bond reconstruction, *J. Appl. Phys.*, 106:014308, 2009.

49. R. Lake and S. Datta, Nonequilibrium Green's-function method applied to double-barrier resonant-tunneling diodes, *Phys. Rev. B*, 45:6670–6686, 1992.

50. D. Singh, J. Y. Murthy, and T. S. Fisher, Effect of phonon dispersion on thermal conduction across Si/Ge interfaces, *J. Heat Transfer*, 133:122401, 2011.

51. X. Gonze, Perturbation expansion of variational principles at arbitrary order, *Phys. Rev. A*, 52:1086–1095, 1995.

52. X. Gonze, Adiabatic density-functional perturbation theory, *Phys. Rev. A*, 52:1096–1114, 1995.

53. E. Isaev, S. Simak, I. Abrikosov, R. Ahuja, Y. K. Vekilov, M. Katsnelson, A. Lichtenstein, and B. Johansson, Phonon related properties of transition metals, their carbides, and nitrides: A first-principles study, *J. Appl. Phys.*, 101:123519, 2007.

54. R. Gillen, M. Mohr, C. Thomsen, and J. Maultzsch, Vibrational properties of graphene nanoribbons by first-principles calculations, *Phys. Rev. B*, 80:155418, 2009.

55. R. Miwa, W. Orellana, and A. Fazzio, Substrate-dependent electronic properties of an armchair carbon nanotube adsorbed on H/Si(001), *Appl. Phys. Lett.*, 86:213111, 2005.

56. S. Barraza-Lopez, P. M. Albrecht, N. A. Romero, and K. Hess, Ab initio study of semiconducting carbon nanotubes adsorbed on the Si(100) surface: Diameter- and registration-dependent atomic configurations and electronic properties, *J. Appl. Phys.*, 100:124304, 2006.

57. K. Stokbro, J. Taylor, M. Brandbyge, and P. Ordejon, Transiesta: A spice for molecular electronics, *Ann. N.Y. Acad. Sci.*, 1006:212–226, 2003.

58. W. A. Harrison, *Electronic Structure and the Properties of Solids*, Dover, New York, 1989.

59. C. Chen and J.-H. Wang, The relation of the Gruneisen parameter to the fractal dimension, *Physica B*, 299:194–197, 2001.

60. P. Kim, L. Shi, A. Majumdar, and P. McEuen, Thermal transport measurements of individual multiwalled nanotubes, *Phys. Rev. Lett.*, 87:215502, 2001.

61. B. A. Cola, J. Xu, C. Cheng, X. Xu, T. S. Fisher, and H. Hu, Photoacoustic characterization of

carbon nanotube array thermal interfaces, *J. Appl. Phys.*, 101:054313, 2007.

62. G. Mahan and G. S. Jeon, Flexure modes in carbon nanotubes, *Phys. Rev. B*, 70:075405, 2004.
63. N. Mounet and N. Marzari, First-principles determination of the structural, vibrational and thermodynamic properties of diamond, graphite, and derivatives, *Phys. Rev. B*, 71:205214, 2005.
64. Z. Huang, D. Singh, J. Murthy, and T. Fisher, Boltzmann transport equation simulation of semiconductor interfacial heat transfer based on input from the atomistic Green's function method, *MRS Proc.*, p. 1172, 2009.
65. S. Lee, D. G. Cahill, and R. Venkatasubramanian, Thermal conductivity of Si-Ge superlattices, *Appl. Phys. Lett.*, 70:2957–2959, 1997.
66. T. Borca-Tasciuc, W. Liu, J. Liu, T. Zeng, D. W. Song, C. D. Moore, G. Chen, K. L. Wang, M. S. Goorsky, T. Radetic, R. Gronsky, T. Koga, and M. S. Dresselhaus, Thermal conductivity of symmetrically strained Si/Ge superlattices, *Superlattices Microstruct.*, 28:199–206, 2000.
67. D. Li, Y. Wu, R. Fan, P. Yang, and A. Majumdar, Thermal conductivity of Si/SiGe superlattice nanowires, *Appl. Phys. Lett.*, 83:3186–3188, 2003.
68. B. Yang and G. Chen, Partially coherent phonon heat conduction in superlattices, *Phys. Rev. B*, 67:195311, 2003.
69. Y. Ezzahri, S. Grauby, S. Dilhaire, J. M. Rampnoux, and W. Claeys, Cross-plan Si/SiGe superlattice acoustic and thermal properties measurement by picosecond ultrasonics, *J. Appl. Phys.*, 101:013705, 2007.
70. C.-K. Liu, C.-K. Yu, H.-C. Chien, S.-L. Kuo, C.-Y. Hsu, M.-J. Dai, G.-L. Luo, S.-C. Huang, and M.-J. Huang, Thermal conductivity of Si/SiGe superlattice films, *J. Appl. Phys.*, 104:114301, 2008.
71. J. D. Jeffers, K. Namjou, Z. Cai, P. J. McCann, and L. Olona, Cross-plane thermal conductivity of a PbSnSe/PbSe superlattice material, *Appl. Phys. Lett.*, 99:041903, 2011.
72. M. N. Luckyanova, J. Garg, K. Esfarjani, A. Jandl, M. T. Bulsara, A. J. Schmidt, A. J. Minnich, S. Chen, M. S. Dresselhaus, Z. Ren, E. A. Fitzgerald, and G. Chen, Coherent phonon heat conduction in superlattices, *Science*, 338:936–939, 2012.
73. D. Li, Y. Wu, P. Kim, L. Shi, P. Yang, and A. Majumdar, Thermal conductivity of individual silicon nanowires, *Appl. Phys. Lett.*, 83:2934–2936, 2003.
74. N. Stojanovic, J. M. Berg, D. H. S. Maithripala, and M. Holtz, Direct measurement of thermal conductivity of aluminum nanowires, *Appl. Phys. Lett.*, 95:091905, 2009.
75. M. C. Wingert, Z. C. Y. Chen, E. Dechaumphai, J. Moon, J.-H. Kim, J. Xiang, and R. Chen, Thermal conductivity of Ge and Ge-Si core-shell nanowires in the phonon confinement regime, *Nano Lett.*, 11:5507–5513, 2011.
76. L. Yin, E. K. Lee, J. W. Lee, D. Whang, B. L. Choi, and C. Yu, The influence of phonon scatterings on the thermal conductivity of SiGe nanowires, *Appl. Phys. Lett.*, 101:043114, 2012.
77. W. Cai, A. L. Moore, Y. Zhu, X. Li, S. Chen, L. Shi, and R. S. Ruoff, Thermal transport in suspended and supported monolayer graphene grown by chemical vapor deposition, *Nano Lett.*, 10:1645–1651, 2010.
78. P. E. Hopkins, M. Baraket, E. V. Barnat, T. E. Beechem, S. P. Kearney, J. C. Duda, J. T. Robinson, and S. G. Walton, Manipulating thermal conductance at metal-graphene contacts via chemical functionalization, *Nano Lett.*, 12:590–595, 2012.
79. X. J. Hu, A. A. Padilla, J. Xu, T. S. Fisher, and K. E. Goodson, 3-omega measurements of

vertically oriented carbon nanotubes on silicon, *J. Heat Transfer*, 128:1109–1113, 2006.

80. Y. K. Koh, M.-H. Bae, D. G. Cahill, and E. Pop, Heat conduction across monolayer and few-layer graphenes, *Nano Lett.*, 10:4363–4368, 2010.
81. P. M. Norris, J. L. Smoyer, J. C. Duda, and P. E. Hopkins, Prediction and measurement of thermal transport across interfaces between isotropic solids and graphitic materials, *ASME J. Heat Transfer*, 134:020910, 2012.
82. A. J. Schmidt, K. C. Collins, A. J. Minnich, and G. Chen, Thermal conductance and phonon transmissivity of metal–graphite interfaces, *J. Appl. Phys.*, 107:104907, 2010.
83. T. Tong, Y. Zhao, L. Delzeit, A. Kashani, M. Meyyappan, and A. Majumdar, Dense vertically aligned multiwalled carbon nanotube arrays as thermal interface materials, *IEEE Trans. Components Packag. Technol.*, 30:92–100, 2007.
84. K. Zhang, Y. Chai, M. Yuen, D. Xiao, and P. Chan, Carbon nanotube thermal interface material for high-brightness light-emitting-diode cooling, *Nanotechnology*, 19:215706, 2008.
85. Z. Chen, W. Jang, W. Bao, C. N. Lau, and C. Dames, Thermal contact resistance between graphene and silicon dioxide, *Appl. Phys. Lett.*, 95:161910, 2009.
86. J. J. Gengler, S. V. Shenogin, J. E. Bultman, A. K. Roy, A. A. Voevodin, and C. Muratore, Limited thermal conductance of metal-carbon interfaces, *J. Appl. Phys.*, 112:094904, 2012.
87. L. Chen, Z. Huang, and S. Kumar, Phonon transmission and thermal conductance across graphene/Cu interface, *Appl. Phys. Lett.*, 103:123110, 2013.
88. I. Srivastava, S. Sadasivam, K. C. Smith, and T. S. Fisher, Combined microstructure and heat conduction modeling of heterogeneous interfaces and materials, *ASME J. Heat Transfer*, 135:061603, 2013.